Economic Geology, v. 103, pp. 405–424

Origin and Evolution of the Um Egat and Dungash Orogenic Gold Deposits, Egyptian Eastern Desert: Evidence from Fluid Inclusions in Quartz

B. A. Zoheir,

Department of Geology, Benha Faculty of Science, Benha 13518, Egypt

A. K. El-Shazly,†

Geology Department, Marshall University, Huntington, West Virginia 25725

H. Helba, K. I. Khalil,

Geology Department, University of Alexandria, Alexandria, Egypt

and R. J. Bodnar

Department of Geosciences, Virginia Tech, Blacksburg,Virginia 24061

Abstract

Shear zone-related, mesothermal gold deposits of Um Egat and Dungash in the Egyptian Eastern Desert are hosted by greenschist facies metavolcanic and/or metasedimentary rocks of Pan-African age. Both deposits comprise boudinaged quartz veins that show evidence of incipient recrystallization, and are similar in alteration style, structural control, and mineralogy. The ore mineralogy includes pyrite, arsenopyrite ± pyrrhotite ± chalcopyrite ± galena; gold occurs both in the veins, usually included in arsenopyrite, pyrite, or pyrrhotite next to fragments of altered country rocks, or disseminated in the alteration haloes. Arsenic in arsenopyrite and Al^{iv} in chlorite geothermometers indicate that wall-rock alteration and ore mineral precipitation occurred at temperatures between 400° and 250°C.

Fluid inclusions in vein quartz occur in clusters, or along trails. Three types of fluid inclusions were identified based on petrography and laser micro-Raman spectroscopy: (1) two-phase carbonic inclusions with CO_2 + CH_4 ± N_2 ± H_2O, (2) two-phase aqueous inclusions, and (3) three-phase aqueous-carbonic inclusions with CH_4. Final melting of ice (Tm_f) for most inclusions occurs at temperatures between –4° and 0°C, indicating a low salinity (<6.5 wt % NaCl equiv) for the aqueous fluid. Homogenization temperatures (T_h) for the two-phase aqueous and aqueous-carbonic inclusions range from 120° to >300°C, but cluster into two distinct groups for each type of inclusion. Inclusions from the same trail or cluster are commonly characterized by different degrees of fill or different T_h values.

Field, petrographic, and microthermometric data suggest that low-salinity aqueous-carbonic fluids interacted with graphite-bearing metasedimentary rocks to form CH_4 at T >400°C and P >3 kbars. These reduced fluids leached gold as they circulated through the metavolcanic rocks, carrying it in the form of bisulfide complexes. Interaction of these aqueous-carbonic fluids with the country rocks caused hydrothermal alteration and precipitated gold-bearing sulfides in the alteration zones. A drop of pressure during the migration of these fluids to shallower depths along the shear zones led to phase separation at T ≤300°C and P ≤2.3 kbars. Quartz crystallizing over a range of lower temperatures and pressures trapped carbonic and aqueous fluids as separate inclusions in clusters along pseudosecondary and secondary trails. Postdepositional deformation caused decrepitation of some inclusions, and the stretching and leakage of others, increasing T_h to >250°C. Deformation also remobilized the gold, depositing it as globules of higher fineness in secondary sites.

Introduction

Neoproterozoic rocks of the Arabian-Nubian shield exposed in the Eastern Desert of Egypt have long been known to host gold, with more than 95 occurrences so far identified (e.g., Kochine and Bassuni, 1968; Botros, 2002; Fig. 1). Most of these occurrences are considered hydrothermal vein-type deposits. These veins crosscut either greenschist facies metavolcanic and metasedimentary rocks, or mostly unmetamorphosed granite, diorite, and gabbro intrusions (e.g., El-Ramly et al., 1970; Hassan and Hashad, 1990; Hussein, 1990; Botros, 2004). Most of the intrusive rocks of the Eastern Desert are products of multiple episodes of magmatic activity broadly grouped into two main events: an "old" (850–614 Ma) event of calc-alkalic granitoids and a "young" (603–575 Ma) event dominated by alkalic granites (e.g., El-Gaby et al., 1990, and references therein).

Although most of the hydrothermal vein gold deposits were extensively mined between 1902 and 1958, with several currently being reworked or considered for mining, their origin and conditions of formation remain controversial. Several authors suggested that the gold mineralization was related to the intrusion of the "younger" (postorogenic) granites into older basement rocks (e.g., Amin, 1955; El-Shazly, 1957; and Klemm et al., 2001). Klemm et al. (2001) further added that gold was deposited at temperatures of 300° to 400°C and pressures of 1 to 2 kbars. This conclusion was supported by Harraz (2000, 2002), based on studies of deposits at El-Sid and Atud (deposits 10 and 14, respectively, in Fig. 1). Other

† Corresponding author: e-mail, elshazly@marshall.edu

0361-0128/08/3732/405-20

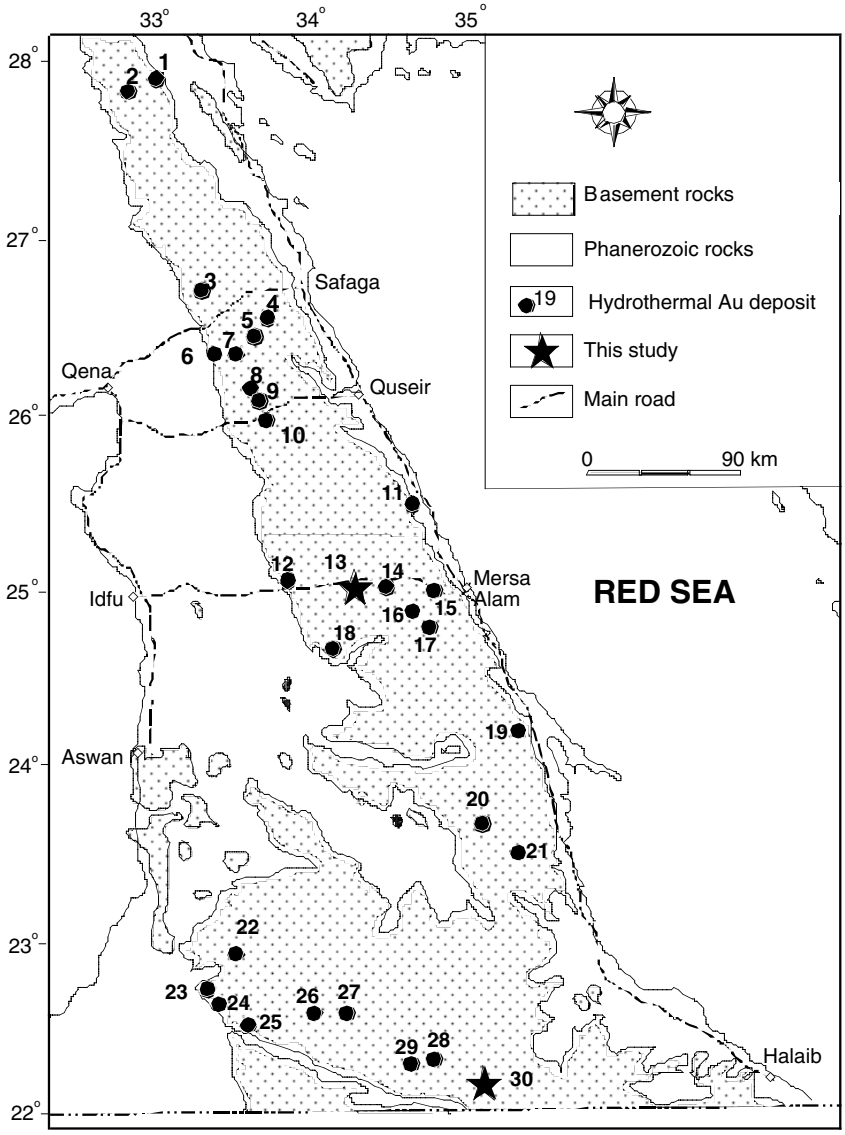

FIG. 1. Locations of the representative vein-type gold deposits in the Eastern Desert of Egypt (compiled from Kochine and Bassuni, 1968; El-Ramly et al., 1970). 1 = Um Mongul, 2 = Um Balad, 3 = Fatira, 4 = Abu Marawat, 5 = Semma, 6 = Hamana, 7 = Erediya, 8 = Atalla, 9 = Fawakhir, 10 = El Sid, 11 = Um Rus, 12 = Barramiya, 13 = Dungash, 14 = Atud, 15 = Sukkari, 16 = Hanglaliya, 17 = Um Ud, 18 = Hamash, 19 = Abu Rahaya, 20 = Um Eleiga, 21 = Hutit, 22 = Hariari, 23 = Haimur, 24 = Um Garaiart, 25 = Atshani, 26 = Murra, 27 = Seiga, 28 = Umm Tuyur, 29 = Betam, 30 = Um Egat. Solid stars highlight the locations of Um Egat and Dungash.

authors interpret these deposits as products of hydrothermal activity induced either by metamorphic or cooling effects of early Paleozoic magmatism (e.g., Pohl, 1988) or Early Cambrian subduction-related calc-alkalic magmatism (El Gaby et al., 1988). Almond et al. (1984) suggested that gold deposition was related to an episode of shearing that postdated the emplacement of all batholithic intrusions but may have been coeval with regional cooling. On the other hand, Hussein (1990) argued that most of these hydrothermal vein deposits are epithermal rather than mesothermal.

In all cases, gold in these hydrothermal veins is considered to have been leached either from the host metabasalts or from nearby ultramafic rocks. Although the source of the hydrothermal fluids that leached and transported the gold may have differed from one area to another, most authors seem to favor either a metamorphic origin (e.g., Hassaan and El-Mezayen, 1995) or a combined metamorphic-magmatic origin (e.g., Harraz, 2000; Klemm et al., 2001; Botros, 2002, 2004) for these fluids. Spatial and temporal relationships between gold veins and structures in the Arabian Nubian Shield have led many authors to suggest a genetic relationship between mineralization and major tectonic events such as the Late Pan-African transpression (e.g., Sabet and Bondonosov, 1984; Harraz and Ashmawy, 1994; Loizenbauer and Neumayr, 1996).

Resolving some of the genetic problems of these gold deposits requires detailed mineralogical and chemical studies of the hydrothermal veins and their alteration zones, as well as fluid inclusion analysis. In this paper, we present petrographic

and chemical data for minerals, and preliminary microthermometric measurements and micro-Raman analyses of fluid inclusions in quartz from two hydrothermal gold-bearing veins in the Eastern Desert of Egypt, namely, the Dungash and Um Egat deposits (13 and 30, respectively, in Fig. 1). Both deposits have been the subject of recent studies that focused on their structural and/or petrological relations (e.g., Helba et al., 2001; Khalil et al., 2003; Zoheir, 2004; Zoheir and Klemm, 2007), but no information is available on the composition of the mineralizing fluids and their evolution. In this study, we present petrographic, microthermometric, and laser infrared micro-Raman data on fluid inclusions in quartz from some of the samples studied by Helba et al. (2001) and Zoheir (2004) in order to accomplish the following: (1) compare these two gold-bearing deposits in terms of structures, textures, and mineralogy, (2) constrain the minimum temperatures (and pressures) of vein formation, hydrothermal alteration, and gold deposition, (3) constrain the compositions and salinities of the vein-forming fluids, (4) provide genetic models for these two deposits (e.g., orogenic as defined by Groves et al., 1998, or intrusion-related in the sense of Lang and Baker, 2001), and (5) provide a better understanding of hydrothermal gold mineralization in general throughout the Egyptian Eastern Desert.

Geologic Setting

The Um Egat and Dungash deposits of the Eastern Desert of Egypt are both hosted by Neoproterozoic greenschist facies metavolcanic and metasedimentary rocks that are tectonically overlain by ophiolitic slices emplaced during an arc–back-arc collisional event (e.g., Stern, 1981; Morgan, 1990). In both areas, the greenschist facies metamorphic rocks are intruded by calc-alkalic and alkalic granitic rocks. Gold deposits occur along postmetamorphic brittle-ductile shear zones (Figs. 2–5). Along these shear zones, quartz veins show an anastomozing and undulating geometry, both

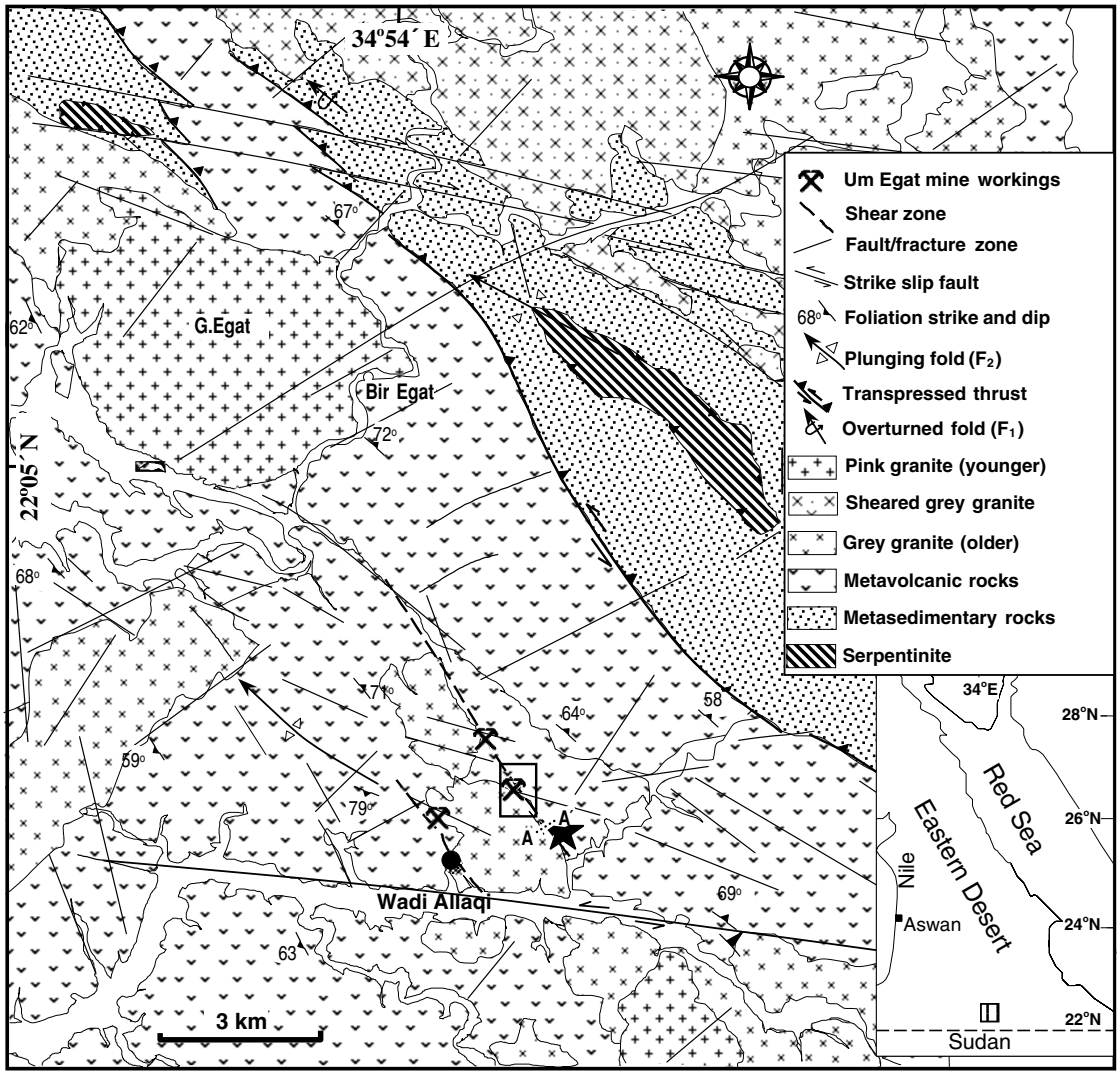

FIG. 2. Simplified geologic map of Um Egat showing the location of the mine and the various shear zones. A-A' represents the line of section shown in Figure 3a, whereas the rectangle outlines the area of the map shown in Figure 3b. Solid star indicates the location of samples R-20 and R-21; solid circle that of sample R-22. Shaded box on the inset map shows the location of the map area of Gebel Egat.

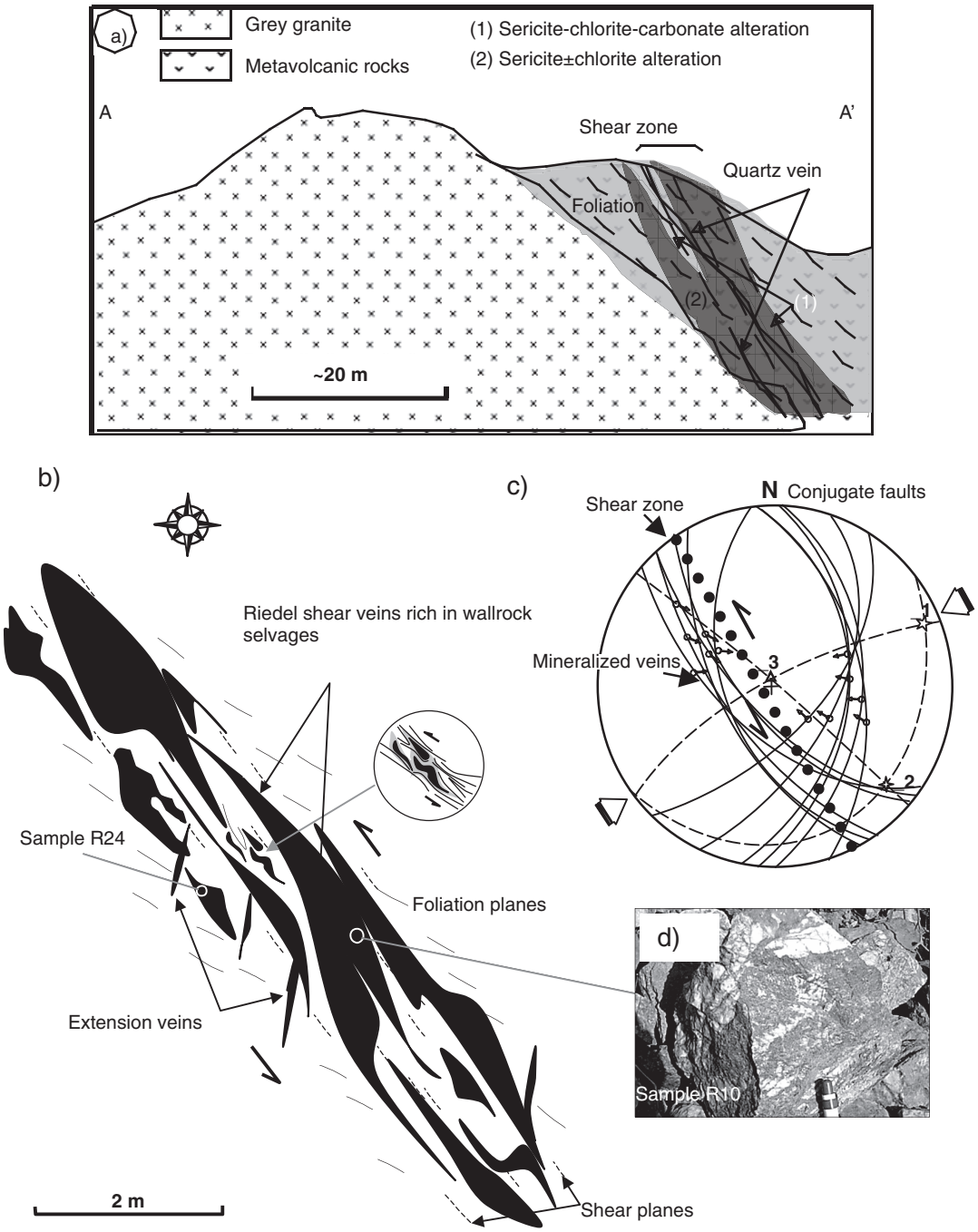

FIG. 3. (a) Schematic cross section based on field observations showing the geometric relationships between the shear zone (and associated quartz veins), country rock foliation and contact of the granite body, looking west-northwest, drawn along line A-A' of Figure 2. (b) Geometry of the Au-mineralized shear zone at the Um Egat mine; shown through a sketch map based on field observations. The Riedel-type veins intersect the foliation at small acute angles. Quartz boudin asymmetry, foliation deflection into the shear planes, and S-type rootless folds indicate a sinistral sense of shear. (c) Analysis of fault planes and conjugate faults, slickensides, and stretching lineations, indicating compressional transpression-induced shearing. (d) Field view of location of sample R-10, showing quartz intermingled with ferruginous, chloritized, and silicified metavolcanic rocks.

downdip and along strike. Single reefs may bifurcate to form two separate veins, which collectively form dense networks of quartz veinlets along strike (e.g., Figs. 3b, 6a). The bifurcating quartz veins are commonly separated by highly deformed, strongly altered mafic schists. The characteristics of these two deposits are summarized below and in Table 1.

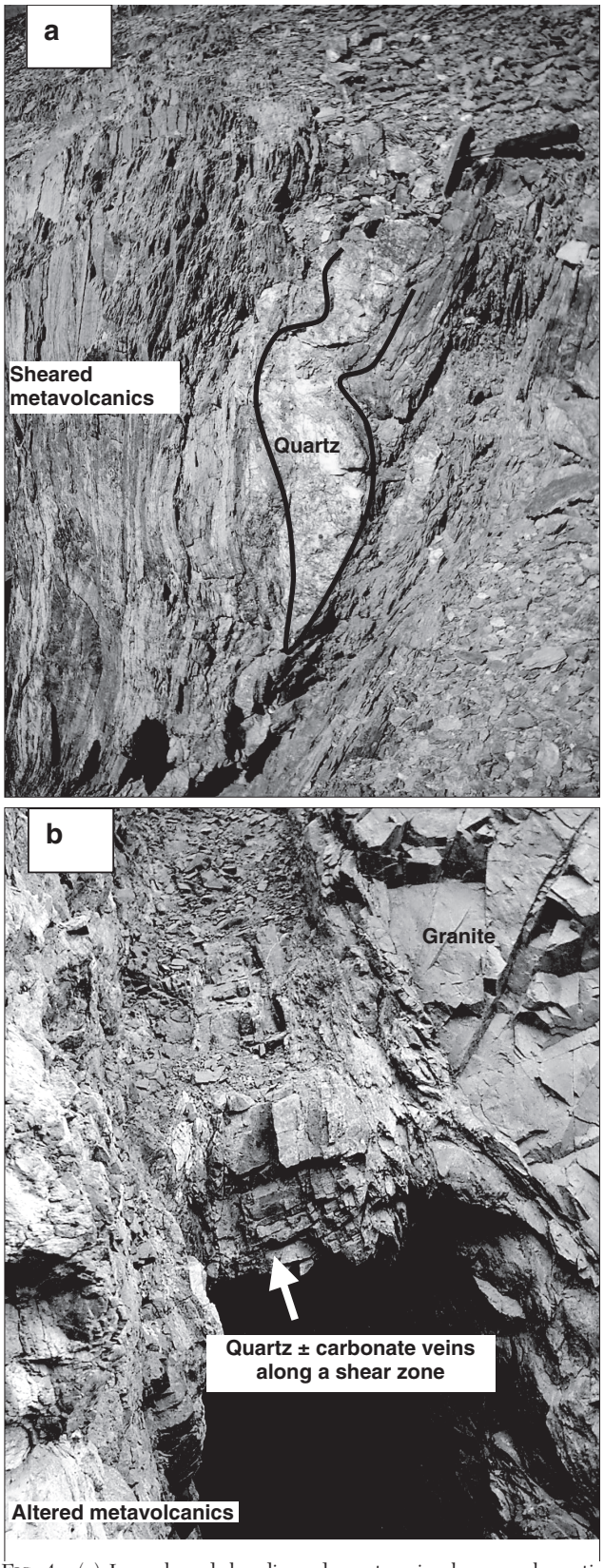

FIG. 4. (a) Lens-shaped, boudinaged quartz vein along nearly vertical shear foliation at the Um Egat mine area (looking south). (b) Quartz ± carbonate veins along narrow shear zones occupying a steeply dipping contact between the country metavolcanic rocks and sericitized granite at the Um Egat mine area (looking south).

Um Egat area

The Um Egat deposit (22°03' N, 34°54' E) is located close to Egypt's border with Sudan (Fig. 1). The veins crosscut a sequence of highly deformed greenschist facies rocks with a prominent foliation striking northwest-southeast. The protoliths of these rocks are predominantly mafic volcanic rocks that represent part of a Late Proterozoic island arc suite (El Shimi, 1996). These metavolcanic rocks are overthrust by metasedimentary rocks and serpentinites interpreted as part of a melange with ophiolitic slices (Zoheir, 2004; Zoheir and Klemm, 2007). The metavolcanic and metasedimentary sequences are intruded by a gray granite (locally granodioritic in composition) known as the "older" granite (850–615 Ma). Both the metamorphic and intrusive granitic rocks were affected by shearing, especially close to the faults and contacts between the metavolcanic rocks and the granites (Fig. 2). Although these shear zones clearly cut across both rock types (Fig. 3a), shearing is more prominently developed in the metavolcanic rocks (Fig. 4a, b). The metamorphic rocks are also intruded by a pink granite ("younger granite": 620–530 Ma) that forms conspicuous peaks like Gebel Egat. These pink granite intrusions are almost undeformed and cut across most structural fabrics in the area, indicating that their emplacement postdates metamorphism and the most prominent deformational events.

The Um Egat area was affected by three major deformational events represented by (1) overturned to recumbent F_1 folds plunging to the northwest, (2) inclined F_2 folds associated with penetrative, steeply dipping axial planar foliation, and sinistral faults and shear zones with northwest-southeast strikes, and (3) right-lateral north-northwest–south-southeast strike-slip faults and associated brittle-ductile shear zones (Zoheir and Klemm, 2007). The mine area is also dissected by several sets of northeast-southwest and west-northwest–east-southeast strike-slip faults, and characterized by minor displacement (Fig. 2).

The northwest-southeast–trending shear zones of the second deformational event cut across the foliation and the sinistral strike-slip faults (Fig. 2) and are interpreted as belonging to the large brittle-ductile shear zones that are well developed throughout the Eastern Desert of Egypt and Sudan (e.g., Greaves and Little, 1929). Gold mineralization is confined to the metavolcanic rocks at the intersection of the northwest-southeast–trending shear zones and the steeply dipping foliation, particularly along the contact with the gray granites (Fig. 3a-c). Because shearing clearly postdated the intrusion of the "older" gray granite (Figs. 3a, 4b), the concentration of shear zones along the contact between the granite and the metavolcanic rocks is interpreted as resulting from the differences in strength of these two rock types.

The mineralized quartz (± carbonate) veins are hosted by the shear zones in discontinuous lenticular bodies that extend up to 1,200 m along strike and are 0.6 to 3.25 m wide. Veinlets of barren quartz (open-space filling; calcite-rich, and relatively poor in wall-rock fragments) overprint the mineralized quartz veins at fault-fracture intersections. Microfolds and asymmetric strain shadows indicate ductile deformation of the veins, whereas grain-size reduction, fracturing, and abrupt displacement of markers in the wall rock suggest brittle deformation. Analysis of structural fabrics, including a

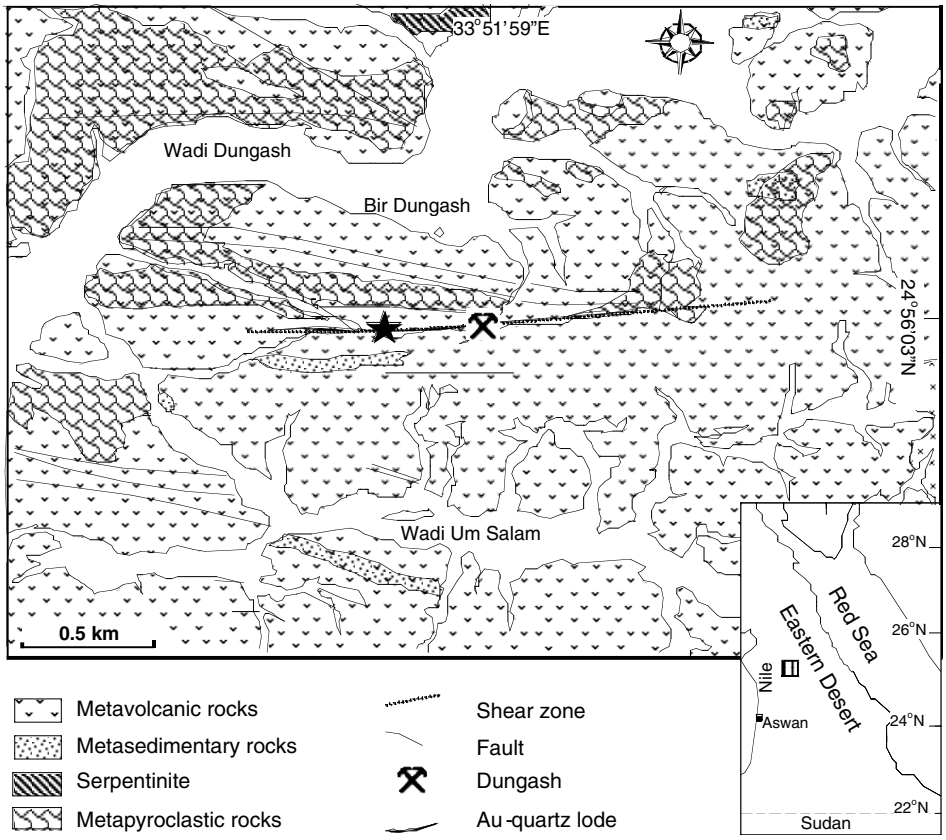

FIG. 5. Simplified geologic map of the Dungash mine area modified after Helba et al. (2001). Solid star denotes the location of the map area of Figure 6a. Note that outcrops of the older granite occur within a few kilometers to the north, west, and south of the map area, whereas the younger granites crop out ~40 km east of the map area (cf. Helba et al., 2001, for a regional scale map). Inset shows the general location of Dungash.

consistent top-to-northwest stretching lineation (defined by chlorite plates and quartz rods), asymmetries, and slickensides on shear planes suggest that these shear zones accommodated an oblique slip, left-lateral, reverse movement (Fig. 3b, c) caused by regional transpression.

The quartz veins are locally fractured and characterized by narrow (0.8–1.2 m) alteration zones of sericite-chlorite-calcite-goethite ± dolomite ± pyrite in the metavolcanic rocks, and sericite ± pyrite replacing the granite. Although a detailed study of the alteration zones around the mineralized quartz vein has yet to be carried out, it is generally observed that the modal content of chlorite in the altered rocks decreases away from the vein more rapidly than sericite. Gold most commonly occurs as inclusions in vein pyrite and arsenopyrite. Gold also occurs as blebs in vein quartz (in close proximity to the sulfides) or as disseminations in the altered wall rocks. The grade of gold in quartz veins ranges from 0.3 to 4 g/ton, whereas that in the hydrothermally altered wall rocks is ≤12 g/t (Oweiss and Said, 2000).

Dungash area

The Dungash mine area (24°56'20" N and 33°51'30" E) is located in the central Eastern Desert, along a 30-km-long desert track running south of the Idfu-Mersa Alam paved road (Fig. 1). The area exposes a sequence of strongly folded metavolcanic and metasedimentary rocks and serpentinites (Fig. 5). This is referred to as the "Meulha-Dungash" mélange sequence and represents remnants of an obducted ophiolite tectonically intermixed with back-arc sedimentary and volcaniclastic rocks later metamorphosed to greenschists (El-Gaby et al., 1990). This sequence was intruded by Neoproterozoic calc-alkalic granites to gabbros ("older" or gray granite), and subalkalic to alkalic granites ("younger" or pink granite), exposed ~1 km west and north, and 40 km to the east of the map area (Fig. 5), respectively. In the mine area, the metavolcanic rocks predominate, ranging in composition from andesite to basaltic andesite with calc-alkalic affinity (Helba et al., 2001). Metapyroclastic rocks are intercalated with the other metavolcanic rocks along their original east-west–striking bedding planes (Fig. 5). A detailed analysis of structures and microfabrics from this area has yet to be carried out.

Gold mineralization occurs in and around an anastomosing, boudinaged, carbonate-bearing quartz vein (Fig. 6a). The vein, which is ~1.5 km long and 0.25 to 4 m thick, crosscuts metavolcanic rocks locally intercalated with a few meter-thick metapyroclastic and metasedimentary layers. It occurs along an east-west–trending shear zone that dips steeply to the north (Fig. 6b). The vein itself is locally brecciated, with fragments of smoky quartz cemented by milky quartz, and contains disseminations of pyrite, arsenopyrite, chalcopyrite,

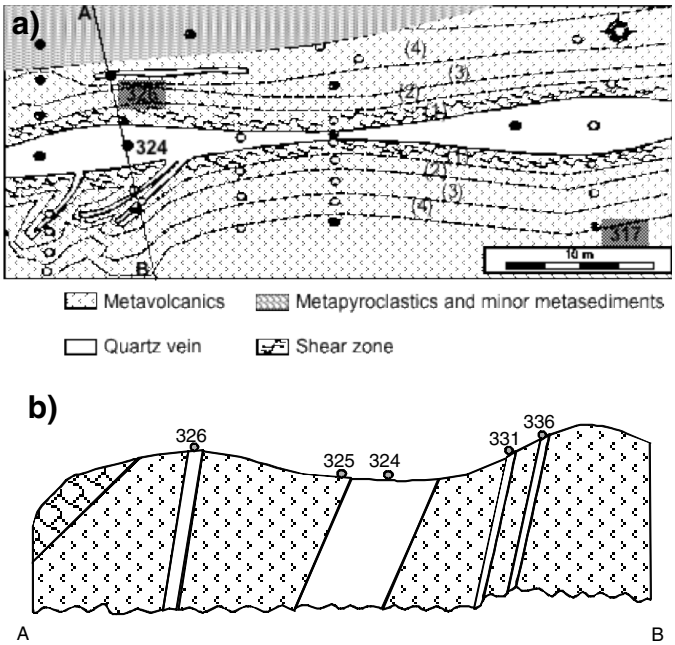

FIG. 6. Sketch map of the quartz vein and shear zone in the area outlined in Figure 5, showing sample locations and alteration patterns. Solid circles indicate the locations of the samples analyzed chemically and presented in Helba et al. (2001); open circles depict locations of samples studied petrographically only. Zones of alteration are delineated by dashed lines and numbered as follows: 1 = silica-sericite zone, 2 = sericite zone, 3 = carbonate-sericite zone, 4 = chlorite-sericite zone. (b) Schematic cross section along line A-B of Figure 6a, showing the locations of some samples discussed in text and in Helba et al. (2001).

galena, carbonates, rutile, anatase, and relics of altered wall rock.

Hydrothermal alteration adjacent to the gold-bearing quartz vein is manifested by an alteration halo with four distinct zones (Fig. 6a)—(1) quartz-sericite, (2) sericite, (3) carbonate-sericite, and (4) chlorite-sericite—in order of increasing distance from the vein margin (Helba et al., 2001). Native gold is disseminated in pyrite and arsenopyrite, both within the vein, as well as in its alteration halo (particularly within the carbonate-sericite zone: Helba et al., 2001; Khalil et al., 2003). Details of the geochemistry and petrography of the vein system and its alteration zones are given in Helba et al. (2001) and Khalil et al. (2003). The average gold content of mineralized veins was determined to range between 1 and 21 g/t in 6 rock chips and grab samples (Egyptian Mineral Resources Authority, 2006).

Petrography and Mineral Parageneses

Um Egat

The most abundant ore minerals of the quartz veins are arsenopyrite and pyrite, with minor amounts of chalcopyrite and galena. Late goethite and siderite (after pyrite?) are also common in the weathered portions of the veins and their wall rocks. The sulfides are mostly restricted to thin wall-rock selvages along vein margins (Fig. 7a). Two textural generations of arsenopyrite are recognized: fine-grained crystals (<1 mm) containing inclusions of chalcopyrite and gold, and medium-grained (>1 mm) crystals devoid of inclusions. Most gold grains are irregular and smaller than 50 μm in longest

TABLE 1. Geological Setting of Auriferous Quartz Veins in Um Egat and Dungash

	Um Egat[1]	Dungash[2]
Host rocks	Metavolcanic + metasedimentary rocks with arc signature; greenschist facies	Metavolcanic + metapyroclastic + metasedimentary rocks of "older arc sequence (Shadli unit)"; greenschist facies
Metamorphism	Greenschist facies	Greenschist facies
Age of the host rock	Unknown, but assumed between 711 and 600 Ma	711 ± 10 Ma
Vein type	Series of lenticular and boudinaged veins; concentrated near contact with granites or dacite sills; fractured; milky Qz	One vein; boudinaged; and brecciated; milky Qz
Vein size	1.2 km long; 0.6–4 m thick	1.5 km long; 0.25–4 m thick
Attitude	NW-SE shear zone	ENE-WSW shear zone
Ore minerals[3]	Asp-Py ± Ccp ± Gn – Au	Py-Asp-Po-Spl-Gn ± Mar ± Mgt ± Au
Gold textures	In Py and Asp; along fractures; as individual blebs in Qz	Inclusions in Py, Po, and Asp
Grade (in veins)	0.3 – 40 ppm	3.87 ppm
Alteration	Distinct; <0.8 m; sericite-chlorite-calcite – goethite ± dolomite ± pyrite	4 distinct zones; Au in carbonate + sericite zone
Asp geothermometry	300°–380°C	320°–400°C
Chlorite geothermometry	220°–270°C	300°–325°C
Average T of vein formation	~340°–250°C	~ 400°?–300°C

[1] From Zoheir, 2004, and references therein
[2] From Khalil et al., 2003, and references therein
[3] Abbreviations: Asp = arsenopyrite, Au = native gold, Ccp = chalcopyrite, Chl = chlorite, Gn = galena, Lo = lollengite, Mar = marcasite, Mgt = magnetite, Po = pyrrhotite, Py = pyrite, Qz = quartz, Spl = sphalerite

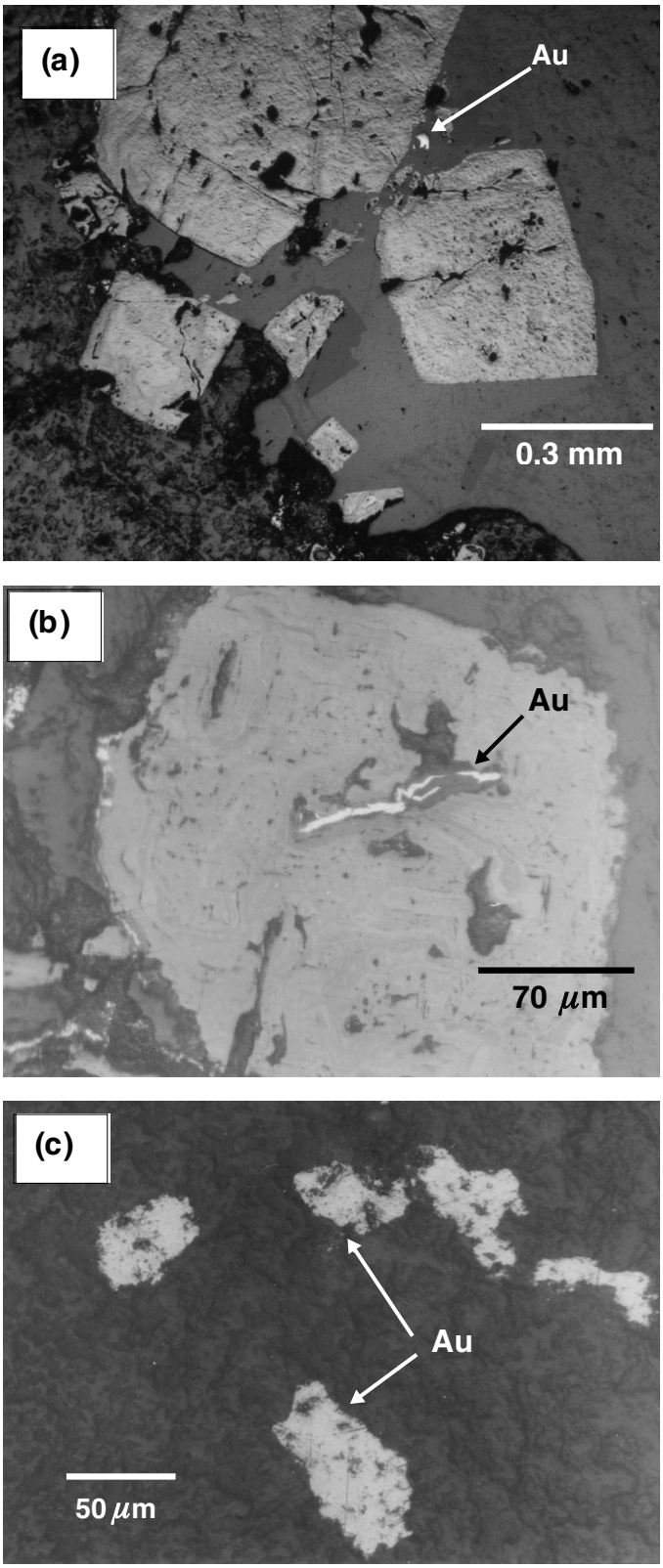

FIG. 7. Photomicrographs of textural relations in Um Egat. (a) Pseudomorphs of goethite after pyrite next to wall-rock selvages, R-24. Note the minute Au speck in quartz (polarized reflected light). (b) Stringers of Au in goethite after pyrite-arsenopyrite (polarized reflected light). (c) Au specks in chlorite from the alteration zone.

dimension. They occur most commonly in, or in close proximity to, arsenopyrite and/or pyrite (Fig. 7a), or along small cracks with late sulfides or oxides replacing the early arsenopyrite in the vein (Fig. 7b). Gold also occurs as irregular blebs and globules (<50 μm) disseminated in the pervasively sericitized and chloritized wall rocks (Fig. 7c).

Dungash

The quartz vein contains calcite, pyrite, pyrrhotite, chalcopyrite, marcasite, galena, and sphalerite. With the exception of sphalerite and marcasite, all these minerals also occur in the altered wall rocks, along with significant amounts of arsenopyrite (the most abundant ore mineral in the alteration zones) and minor chromite, rutile, anatase, and gersdorffite ((Ni,Co,Fe)AsS). Khalil et al. (2003) interpreted chromite, rutile, and anatase as relict magmatic or metamorphic minerals, but concluded that gersdorffite and chalcopyrite were formed with chlorite during the earliest stages of hydrothermal alteration. According to these authors, continued hydrothermal alteration resulted in the sericitization and carbonatization of the country rocks and the precipitation of at least two generations of arsenopyrite, pyrite, pyrrhotite, and gold, with galena and sphalerite forming last. On the other hand, Helba et al. (2001) concluded that the development of the chlorite zone represents the last stage of hydrothermal alteration, following silicification, sericitization, sulfidation, and carbonatization.

Gold occurs (1) as inclusions in medium-grained (~1.5 mm) arsenopyrite in the sericite-carbonate zone of the wall rocks (Helba et al., 2001), (2) as corroded inclusions in vein pyrite (with marcasite, chalcopyrite, and pyrrhotite), and (3) in microfractures in pyrite or along grain boundaries of quartz, especially next to the wall rock (Khalil et al., 2003). Helba et al. (2001) and Khalil et al. (2003) interpreted these textures as indicating the precipitation of gold during the main stage of sulfidation and its remobilization during later sericitization and carbonatization.

Temperatures of Vein Formation and Wall-Rock Alteration

Textural observations and mineral chemical data indicate that these gold-bearing vein systems have had a complex history of wall-rock alteration, fracture infilling, precipitation of vein minerals, and remobilization of gold. Application of some geothermometers to mineral assemblages in the veins and alteration zones helps to constrain the temperatures of vein formation and wall-rock alteration.

Microprobe analyses of chlorite, arsenopyrite, and other ore and gangue minerals were carried out on a CAMECA SX100 electron microprobe at the Institut fur Mineralogie und Mineralisches Rohstoffe, Technische Universitat, Clausthal, Germany (Dungash samples), and a JEOL JSM-6310 electron microprobe at the Institute of Geology and Mineralogy, Graz University, Austria (Um Egat). Operating conditions were 15 kV accelerating voltage, 30 *n*A beam current, and a defocused electron beam with a diameter of 5 to 10 μm. Additional analytical details are given in Khalil et al. (2003) and Zoheir (2004).

For Um Egat, analyses of arsenopyrite (coexisting with pyrite, chalcopyrite, and galena in the quartz veins) indicate

arsenic contents of 28.4 to 30.9 at. wt percent (Table 2). Application of the geothermometer of Kretschmar and Scott (1976) and Scott (1983) to this arsenopyrite-pyrite assemblage yields an average temperature of ~340° ± 30°C, with the fine-grained, gold-bearing arsenopyrite yielding the lower temperature (~300°C) in that range (Fig. 8). Chlorite from the altered wall rocks has Al^{iv} of 1.9 to 2.3 and Fe/(Fe + Mg) of 0.35 to 0.52 (Table 3). Application of the geothermometer of Cathelineau (1988) to these data yields temperatures of ~220° to 270°C for the formation of chlorite.

For Dungash, the occurrence of gersdorffite of composition $(Ni_{0.57}Co_{0.08}Fe_{0.35})AsS$ as an early phase within the alteration zone of the vein led Khalil et al. (2003) to suggest that early alteration occurred at ~500°C, whereas arsenopyrite formed at <300°C, based on the experiments of Klemm (1965). However, the application of the geothermometer of Kretschmar and Scott (1976) constrains the temperature of formation of arsenopyrite (with 28.8–31.7% As; Khalil et al., 2003) first with pyrrhotite (early generation), and then with pyrite (late generation), at ~400° to 320°C (Fig. 8). Application of the chlorite geothermometer of Cathelineau (1988) to wall-rock chlorite yields temperatures of 308° to 325°C (Khalil et al., 2003).

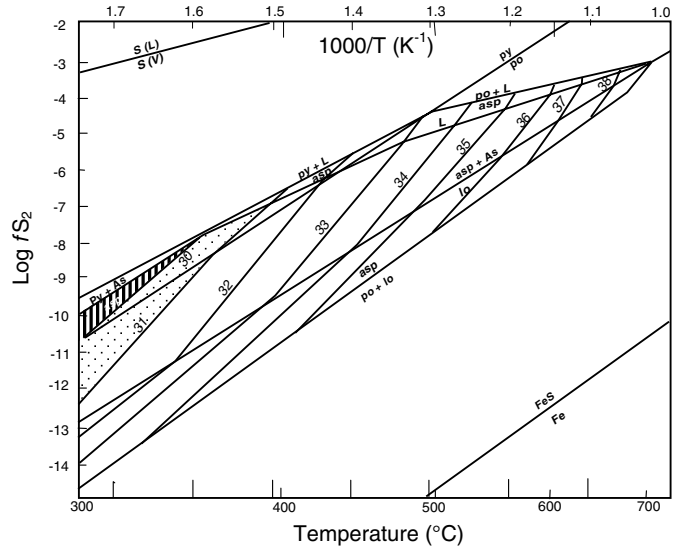

FIG. 8. Log f_{S2}-T projection of the stability of arsenopyrite contoured for atomic wt percent of As (Kretschmar and Scott, 1976). Stippling and vertical ruling mark the conditions of formation of arsenopyrite in Dungash and Um Egat, respectively.

Fluid Inclusion Analysis

Analytical techniques

Fluid inclusion microthermometry was carried out on USGS gas flow-type heating-freezing stages at Rice University and the Fluids Research Lab, Virginia Tech. Freezing experiments were carried out before those of homogenization on the same inclusion to avoid stretching it. Details of the analytical conditions are the same as those used by El-Shazly and Sisson (2004). Laser infrared micro-Raman spectroscopic analysis was carried out on a Jobyn Yvon Horiba LabRam-IR HR 800 spectrometer at the Fluid Research Lab at Virginia Tech. Counting time was 30 seconds for most routine analyses and 60 seconds for the first few analyses.

Vein samples

Um Egat: Five samples of vein quartz were selected for microthermometry. Sample R-10 is from a quartz vein with

TABLE 2. Representative Electron Microprobe Data of Arsenopyrite from Um Egat Au Deposit

Sample no.	1_12	1_14	1-15	1_16	2_16	2_17	2_18	2_19	3_11	3_12	4_11	4_14	4_15	5_11	5_12	5_13
(wt %)																
Fe	35.07	35.55	36.03	35.49	35.86	35.46	35.47	35.35	35.33	35.26	35.49	35.69	35.61	35.59	35.48	35.83
S	22.72	21.35	21.51	21.54	21.59	22.37	21.33	21.92	22.03	23.15	21.46	21.07	21.75	22.12	22.69	21.76
As	42.21	43.10	42.41	42.93	42.38	42.08	42.59	41.26	42.54	41.67	42.35	42.21	42.95	42.19	41.78	42.26
Co	b.d.[1]	0.05	b.d.	b.d.	b.d.	b.d.	b.d.	0.01	0.01	b.d.	b.d.	b.d.	0.03	b.d.	0.03	0.04
Ni	0.01	b.d.	0.03	b.d.	0.03	b.d.	b.d.	0.07	b.d.	b.d.	b.d.	0.06	b.d.	b.d.	0.02	b.d.
Au	b.d.	b.d.	b.d.	b.d.	0.09	b.d.	b.d.	b.d.	b.d.	b.d.	b.d.	0.17	b.d.	b.d.	0.09	0.13
Total	100.01	100.05	99.98	99.96	99.95	99.91	99.39	98.61	99.91	100.08	99.30	99.14	100.34	99.90	100.09	99.98
(at. %)[2]																
Fe	0.99	1.02	1.03	1.01	1.02	1.01	1.02	1.02	1.01	0.99	1.02	1.03	1.01	1.01	1.00	1.02
S	1.12	1.06	1.07	1.07	1.07	1.11	1.07	1.10	1.09	1.13	1.07	1.06	1.08	1.09	1.12	1.08
As	0.89	0.92	0.90	0.91	0.90	0.89	0.91	0.88	0.90	0.87	0.91	0.91	0.91	0.89	0.88	0.90
Co	0.00	0.001	0.00	0.00	0.00	0.00	0.00	0.00	0.000	0.000	0.00	0.00	0.00	0.001	0.00	0.001
Ni	0.00	0.00	0.00	0.00	0.00	0.00	0.00	0.00	0.001	0.00	0.00	0.00	0.002	0.00	0.00	0.00
Au	0.00	0.00	0.00	0.00	0.00	0.00	0.00	0.00	0.00	0.00	0.00	0.00	0.001	0.00	0.00	0.001
Mol%																
FeAsS	99.99	99.95	99.97	100.00	99.95	100.00	100.00	99.93	99.99	100.00	100.00	99.95	99.97	100.00	99.93	99.96
CoAsS	0.00	0.05	0.00	0.00	0.00	0.00	0.00	0.00	0.01	0.00	0.00	0.00	0.03	0.00	0.04	0.04
NiAsS	0.01	0.00	0.03	0.00	0.05	0.00	0.00	0.07	0.00	0.00	0.00	0.05	0.00	0.00	0.03	0.00
T(°C)[3]	331	382	356	375	355	332	373	321	356	302	364	367	369	340	313	347

[1] b.d. = below detection
[2] Mineral formula calculated on the basis of a sum of 3 cations
[3] Temperature estimates based on arsenopyrite-pyrite-arsenic cotectic (in the Fe-Zn-As-S system at 1 bar, after Scott, 1983)

TABLE 3. Representative Chlorite Analyses from Um Egat

Sample no.	1_4	1_5	3_11	3_12	3_13	3_15	3e_2	3e_3	3e_4	27_1	27_2	27_3	27_4	5_3	5_4	5_5	5_9
SiO_2 (wt %)	28.68	29.93	28.16	28.16	29.90	28.46	28.93	29.85	28.89	30.76	30.59	30.00	28.74	29.86	29.53	29.22	30.08
TiO_2	0.00	0.14	0.00	0.00	0.00	0.00	0.00	0.00	0.00	0.05	0.05	0.00	0.00	0.00	0.00	0.00	0.03
Al_2O_3	17.47	18.26	17.20	16.93	17.60	16.90	18.95	15.73	17.68	15.92	15.83	15.39	17.24	17.35	17.80	17.45	16.48
FeO	26.89	24.74	23.75	26.94	23.95	27.01	19.45	24.45	24.13	23.92	22.88	23.61	24.88	21.57	20.07	22.68	23.64
MnO	0.19	0.26	0.34	0.49	0.53	0.23	0.76	0.36	0.47	0.33	0.38	0.46	0.45	0.37	0.45	0.53	0.39
MgO	13.73	14.63	17.15	14.61	16.60	14.41	19.45	17.38	16.59	16.53	17.67	17.66	16.12	18.63	19.58	17.81	16.93
CaO	0.12	0.07	0.12	0.03	0.14	0.24	0.15	0.19	0.09	0.30	0.30	0.29	0.10	0.20	0.21	0.14	0.23
F	0.10	0.02	0.12	<0.01	0.11	<0.01	0.13	<0.01	0.10	0.04	0.05	0.04	0.08	0.10	0.11	0.08	0.06
Total	86.53	87.43	86.20	86.51	88.18	86.60	87.23	87.39	87.30	87.21	87.10	86.80	86.96	87.43	87.11	87.31	87.21
Si[1]	6.11	6.20	5.95	6.02	6.14	6.07	5.89	6.22	6.02	6.38	6.33	6.27	6.04	6.11	6.03	6.04	6.24
Ti	0.00	0.02	0.00	0.00	0.00	0.00	0.00	0.00	0.00	0.01	0.01	0.00	0.00	0.00	0.00	0.00	0.00
$Al^{(iv)}$	1.89	1.80	2.05	1.98	1.86	1.93	2.11	1.78	1.98	1.62	1.67	1.73	1.96	1.89	1.97	1.96	1.76
$Al^{(vi)}$	2.49	2.66	2.23	2.28	2.40	2.32	2.44	2.08	2.36	2.27	2.19	2.06	2.31	2.30	2.32	2.29	2.27
$Fe^{(ii)}$	4.79	4.29	4.19	4.81	4.11	4.82	3.31	4.26	4.20	4.15	3.96	4.13	4.37	3.69	3.43	3.92	4.10
Mn	0.03	0.05	0.06	0.09	0.09	0.04	0.13	0.06	0.08	0.06	0.07	0.08	0.08	0.06	0.08	0.09	0.07
Mg	4.36	4.52	5.40	4.66	5.08	4.58	5.91	5.40	5.15	5.11	5.45	5.50	5.05	5.69	5.96	5.49	5.24
Ca	0.03	0.02	0.03	0.01	0.03	0.05	0.03	0.04	0.02	0.07	0.07	0.06	0.02	0.04	0.05	0.03	0.05
F	0.06	0.01	0.08	0.00	0.07	0.00	0.09	0.00	0.06	0.02	0.03	0.03	0.05	0.06	0.07	0.05	0.04
Total	19.70	19.56	19.91	19.85	19.73	19.81	19.84	19.87	19.81	19.67	19.74	19.83	19.83	19.79	19.83	19.84	19.74
Fe/(Fe+Mg)	0.52	0.49	0.44	0.51	0.45	0.51	0.36	0.44	0.45	0.45	0.42	0.43	0.46	0.39	0.37	0.42	0.44
$Al^{iv2}{}_c$	2.26	2.14	2.36	2.34	2.17	2.29	2.36	2.09	2.30	1.93	1.97	2.03	2.29	2.16	2.22	2.25	2.07
T(°C)[3]	257.46	244.94	267.98	265.73	248.03	260.77	268.02	239.71	261.53	222.89	226.47	233.16	260.45	247.09	253.81	256.55	236.91

[1] Formula calculated on the basis of 28 oxygen atoms using program MINFILE (Afifi and Essene, 1988)
[2] Al^{iv} value corrected following Kranidiotis and McClean (1987)
[3] T calculated using geothermometers of Cathelineau (1988)

selvages of altered wall rock and visible gold, whereas R-20 and R-24 are from lenses of quartz collected from within the alteration zones and are also mineralized (Fig. 3b). Samples R-21 and R-22 are from a younger generation of barren quartz-carbonate veins. Quartz in all samples is strongly deformed, appearing as elongated crystals (~0.1–0.5 mm) with distinct subgrain boundaries, almost always oriented at a high angle to the direction of elongation (Fig. 9a). Grain boundary bulging and incipient recrystallization are clearly developed in most samples (Fig. 9b), indicating deformation by dislocation creep and semibrittle flow (e.g., Tullis, 2002, and references therein). Most fluid inclusions occur along trails, some of which are secondary (crosscutting grain boundaries; Fig. 9c). Most of these secondary trails are subparallel to the direction of elongation of quartz but oriented at a high angle to the subgrain boundaries. Numerous decrepitated inclusions decorate the grain boundaries (Fig. 9d).

Dungash: Three samples were selected for microthermometry. Samples 324 and 326b are from the milky vein quartz, with 326b being more brecciated than 324. Sample 317 is from a vein of quartz + calcite in a brecciated metavolcanic rock (Fig. 6a, b). These samples are characterized by deformational textures quite similar to those of Um Egat, although overall the Dungash samples are more strongly deformed, displaying a more pronounced grain elongation and stronger deformation banding. The Dungash veins are also characterized by a set of distinct late fractures that run parallel to the elongation of the quartz grains. Fluid inclusions occur mostly along pseudosecondary (intragranular) and secondary trails or define the grain boundaries. Most of these inclusions are minute (4–8 μm) and elongated in the direction of the trail (Fig. 10a).

Types of fluid inclusions

Texturally, fluid inclusions occur in clusters in the middle of the quartz crystals, along numerous trails many of which crosscut grain boundaries, and along grain boundaries where they are decrepitated. Although many of the secondary trails intersect, it is very difficult to determine their relative ages. Accordingly, we assume that most of the inclusions along secondary trails formed more or less contemporaneously, either during or shortly after one of the deformational events that were accompanied by quartz recrystallization. Most of these fluid inclusions consist of two phases (liquid and vapor) but are commonly characterized by different degrees of fill (even within the same fluid inclusion assemblage). Based on preliminary microthermometry and laser micro-Raman spectroscopy, three types of inclusions were identified (Table 4).

Type I: Type I inclusions are carbonic, two-phase liquid (L) + vapor (V) inclusions, with variable degrees of fill (10–80 vol % gas). They are small (<10 μm), mostly equant, often with negative crystal shapes, and occur in clusters or along pseudosecondary and secondary trails (Figs. 10b, c; 11a, c). The gas phase is CO_2- CH_4 ± H_2O.

Type II: Type II inclusions are two-phase (L+V) inclusions occurring in clusters and along pseudosecondary or secondary trails, but are characterized by a relatively constant degree of fill for the same fluid inclusion assemblage (FIA, 10–20 vol % gas; Figs. 10d, 11b). Many of these small inclusions (<10 μm) are usually elongated parallel to the direction of their trail (e.g., Fig. 10a). These inclusions are characterized by a predominantly aqueous vapor composition, in some cases with minor CO_2.

Type III: Type III inclusions are relatively large (12–15 μm), highly irregular, three-phase (2 liquids + vapor) inclusions with

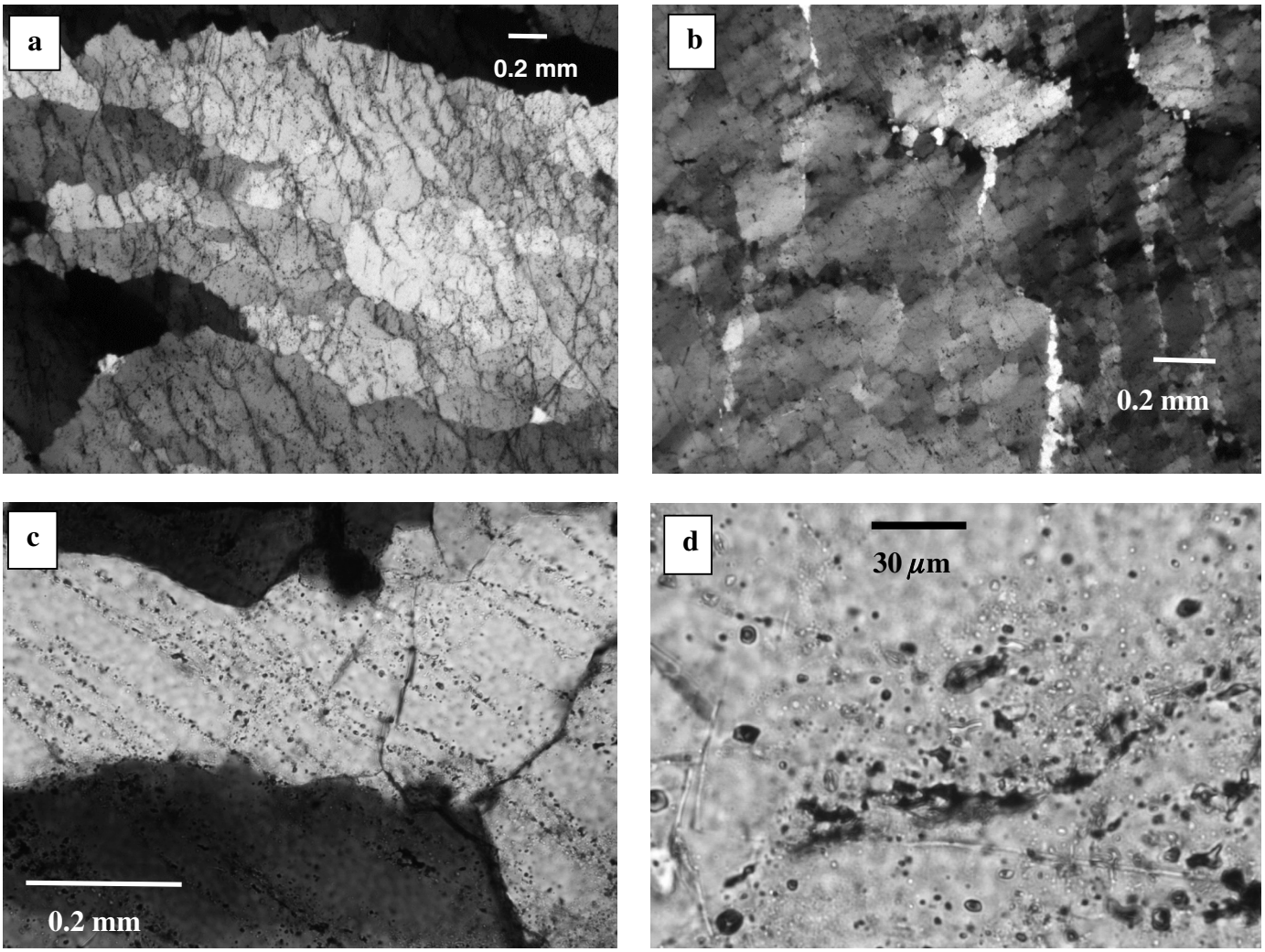

FIG. 9. Deformation textures at Um Egat. (a) Elongated quartz grains showing grain boundary bulging and deformation bands (subgrain rotation crystallization). Note the trails of secondary inclusions. Sample R-22 (cross-polarized light). (b) Incipient recrystallization along quartz grain boundaries. Sample R-10 (cross-polarized light). (c) Fluid inclusion trails crossing grain boundaries (cross-polarized light), sample R-24. (d) Decrepitated inclusions along grain boundaries, sample R-10 (plane-polarized light).

a fairly constant degree of fill (~20 vol % gas). These relatively rare inclusions are either isolated or in clusters (Fig. 11d), and are characterized by a vapor consisting of H_2O-CO_2 ± CH_4.

Microthermometry

Um Egat: More than 60 percent of inclusions in R-10, R-20, R-21, and R-22 are carbonic (type I), with 10 to 35 percent of inclusions of type II, and <5 percent belonging to type III. In contrast, more than 75 percent of the inclusions in sample R-24 are aqueous (type II). In all samples, temperatures of initial melting (Tm_e) for type I inclusions range from –68.5° to –54.2°C, with a median of ca. –64°C, whereas those for type II range from –28° to –21°C. Final ice-melting temperatures (Tm_f) range from –4.8° to 0°C, with most >–3.5°C (Fig. 12). Clathrate-melting temperatures ($Tm_{clathrate}$) were difficult to record and replicate but generally range from 8.2° to ~17 °C (n = 31; median ~11°C) for the carbonic inclusions (types I and III) in samples R-10, R-20, and R-21.

Final homogenization for most inclusions took place through the disappearance of the vapor upon heating (L → V). For type I inclusions, homogenization temperatures range from 200° to ~400°C (with very few outliers in the 120°–200°C range, mostly in the barren veins R-21 and R-22). Nevertheless, T_h values show two distinct modes at 220° to 280°C, and 300° to 360°C (Fig. 13). In general, many type I inclusions with a low degree of fill (~80 vol % gas) hardly show any changes upon heating to temperatures as high as 400°C.

For type II inclusions, homogenization temperatures range from 120° to 300°C with distinct clusters at 140° to 200°C, and 220° to 260°C (Fig. 13). In some samples (e.g., R-10, R-20), T_h values for some inclusions falling on the same trail and/or belonging to the same fluid inclusion assemblage (FIA) differed by as much as 100°C. A few aqueous inclusions in R-10 homogenized through the disappearance of the liquid. For type III inclusions, heating also caused some decrepitation at ~ 285°C (R-20, R-22) and 320°C (R-10, R-24).

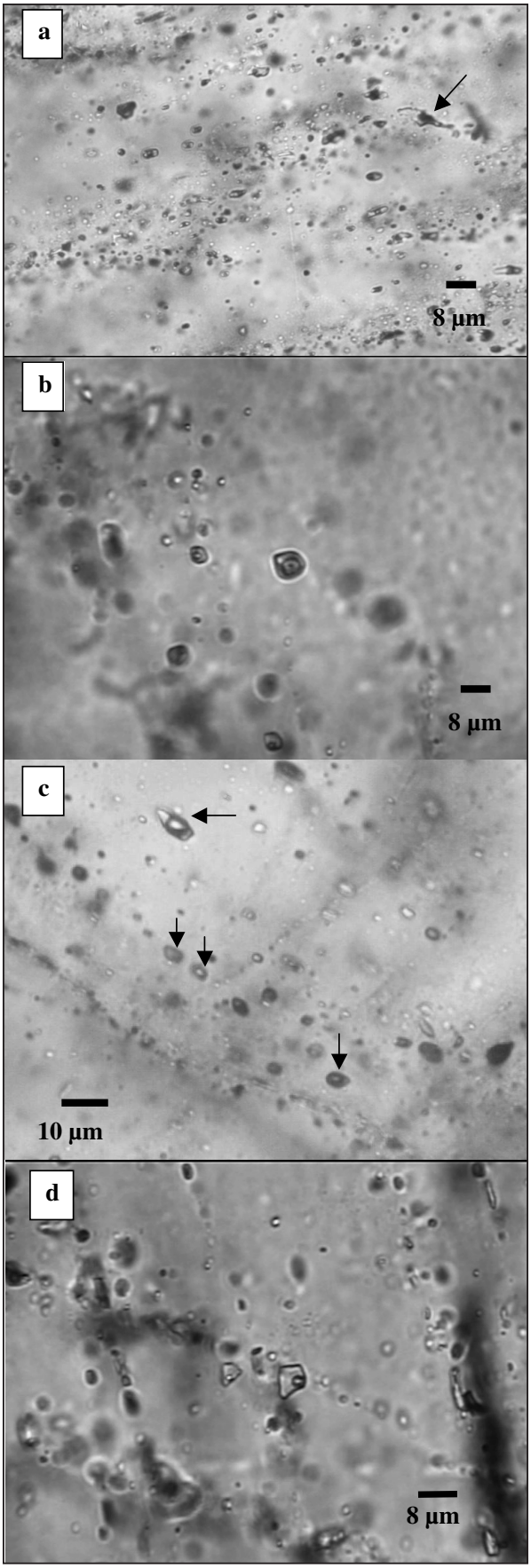

FIG. 10. Selected petrographic relationships of fluid inclusions in samples from Dungash. All photomicrographs taken under plane-polarized light. (a) Minute fluid inclusions along trails; sample 324. Note that most inclusions are elongated parallel to the trail. Arrow points to a type III aqueous-carbonic inclusion. (b) Type I inclusion, sample 326b. (c) Type I carbonic inclusions with low degrees of fill occurring on a trail; sample 324. (d) Type II aqueous inclusion along a trail, sample 326b.

Dungash: 50 to 60 percent of all inclusions in the Dungash samples are predominantly aqueous (type II), typically minute (~3 to 4 μm), thin walled, and elongated in the direction of their trail (Fig. 10a). Of all inclusions, 10 to 35 percent are carbonic (type I), many of which have negative crystal shapes (Fig. 10b), and/or are characterized by low degrees of fill (Fig. 10c). Irregular, three-phase (type III; Fig. 10a) inclusions constitute another 5 to 10 percent of all inclusions.

Temperatures of initial melting of ice range from –64° to –56°C for type I inclusions and –44° to –21.2°C for type II. Tm_f values for both types of inclusions range from –3.8° to 0°C (with the exception of a few lower values recorded for 317; Fig. 14a). This indicates that, whereas type I and II inclusions trap different fluids, the salinity of the aqueous component in both inclusions is quite similar (<6.5 wt % NaCl equiv).

Homogenization temperatures (V → L) for almost all type I inclusions are in excess of 280°C (Fig. 14b). In contrast, T_h values for type II inclusions display two modes at 150° to 200°C, and 220° to 280°C (Fig. 14b). T_h values for some inclusions from the same FIA differ by as much as 200°C. Very few inclusions homogenize through the disappearance of the liquid phase (L → V) at 240° to 315°C. One inclusion in 324 has a T_h of 17.8°C.

Laser micro-Raman results

Analysis of types I, II, and III inclusions from samples R-10 and R-20 (Um Egat) revealed that the vapor phase contains CH_4 + CO_2 ± N_2 ± H_2O (Fig. 15a). The amount of N_2 is minor, and the CO_2/CH_4 varies from one inclusion to another. Type II inclusions are predominantly aqueous with minor amounts of CO_2 (Fig. 15b, c). In the case of the Dungash samples, no N_2 was found in any of the carbonic (type I), aqueous (type II), or aqueous-carbonic (type III) inclusions, and the CO_2/CH_4 ratio was overall higher (Fig. 15d-f). No sulfur compounds or other hydrocarbons were detected in any of the samples analyzed from either area.

Fluid compositions

The large difference (100°–200°C) in T_h values recorded for inclusions within the same FIA, along with variable degrees of fill, and textures that indicate necking down of some of those inclusions (e.g., Fig. 11a) suggests that these inclusions were affected by postentrapment modification and reequilibration. This casts significant doubt on the value of microthermometry for understanding the conditions of veining in Um Egat and Dungash. Nevertheless, each of the samples analyzed has a number of small inclusions within the same FIA that yielded nearly identical T_h, more or less consistent with one of the modes shown on the histograms of Figures 13 and 14b. We therefore argue that some of these T_h values are meaningful and can be helpful in inferring the

TABLE 4. Types of Fluid Inclusions in Vein Quartz

Type	Size (μm)	Shape	Phases	Vol% vapor	Vapor composition	T_h (°C)	Comments
I	<12	Equant	L + V	10–80	CO_2-CH_4 ± N2 ± H_2O	120–300 (Ia) and > 300 (Ia)	Clusters or trails
II	<10	Spindle	L + V	10–20	H_2O ± CO_2	200–300 (IIa) and 120–200 (IIb)	Mostly along trails Secondary trails
III	12–20	Irregular	2L + V	~20	H_2O ± CO_2 ± CH_4	NA	Isolated or in clusters, rare

Abbreviations: L = liquid, V = vapor, T_h = homogenization temperature

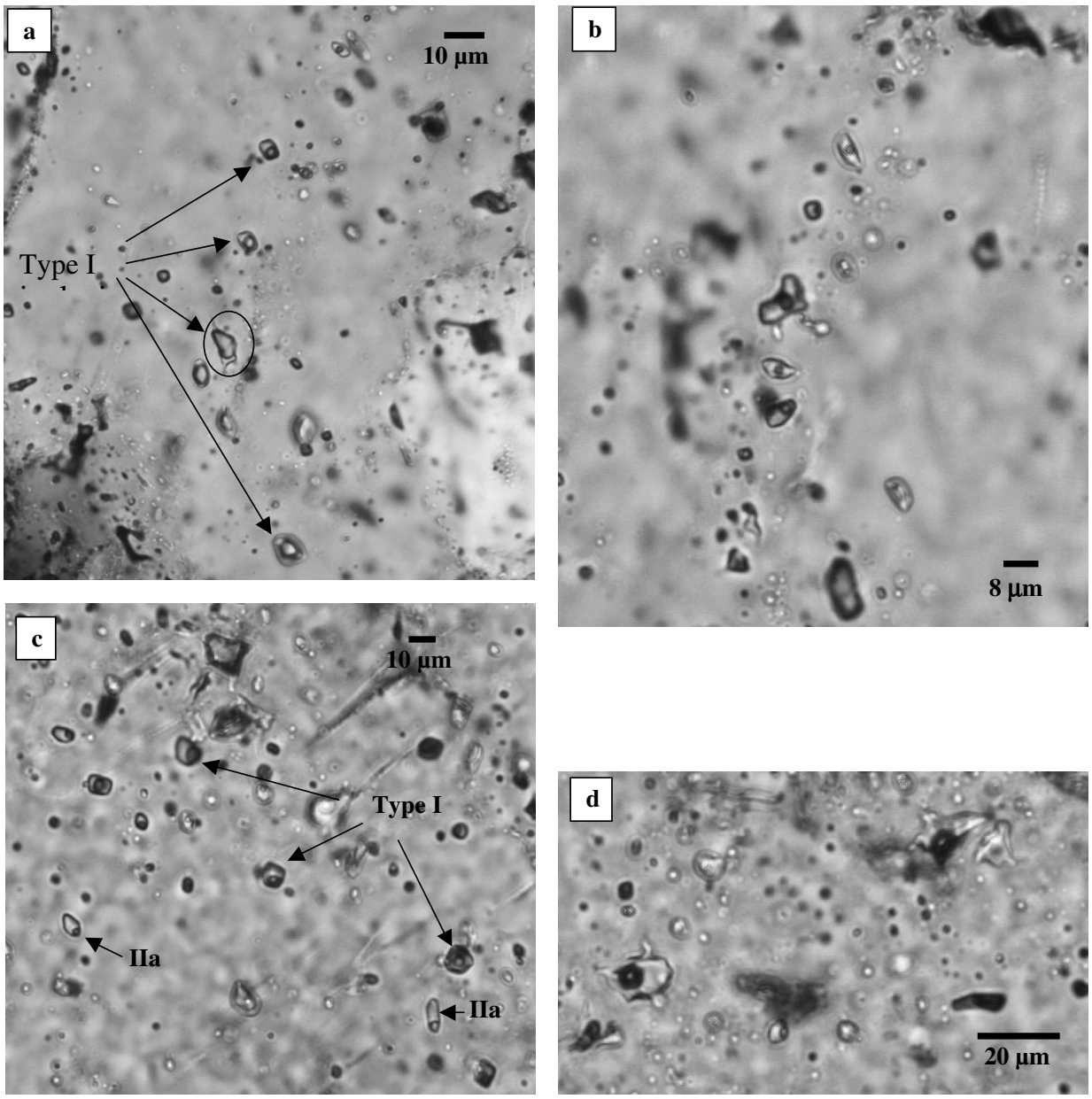

FIG. 11. Fluid inclusions from Um Egat. All photomicrographs in plane-polarized light. (a) Variable degrees of fill in type I inclusions within the same fluid inclusion assemblage. Note the barbed texture (necking down) for the circled inclusion, sample R-22. (b) Trails of fluid inclusions, type II, sample R-22. (c) Types I and II inclusions within the same field of view, and possibly belonging to the same FIA, sample R-22. (d) Type III inclusions, sample R-10.

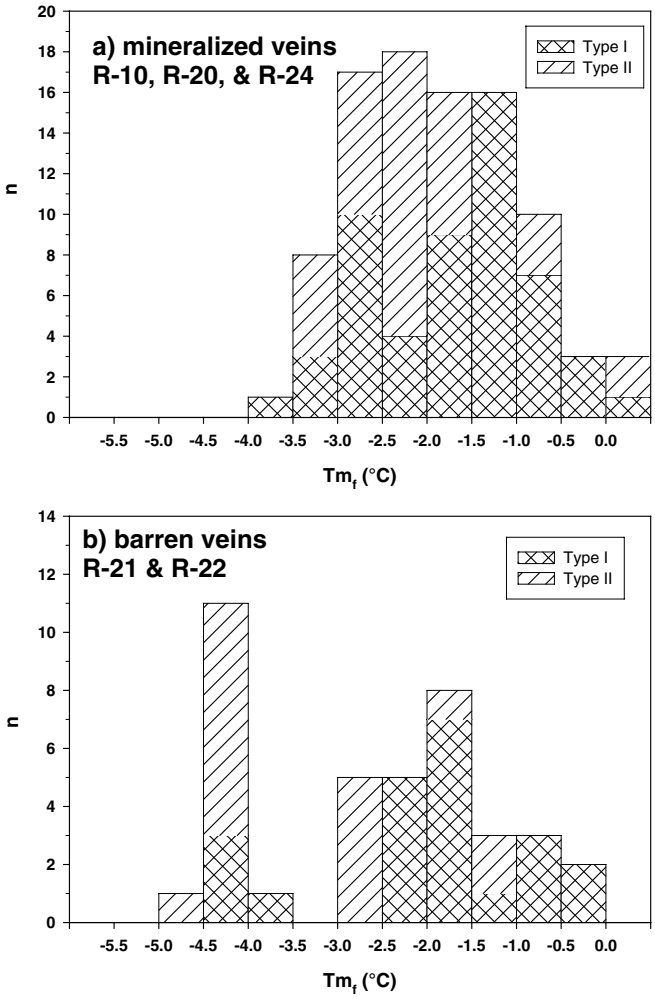

FIG. 12. Histograms showing temperatures of final ice melting (Tm_f) for samples from Um Egat. (a) Mineralized samples. (b) Barren veins.

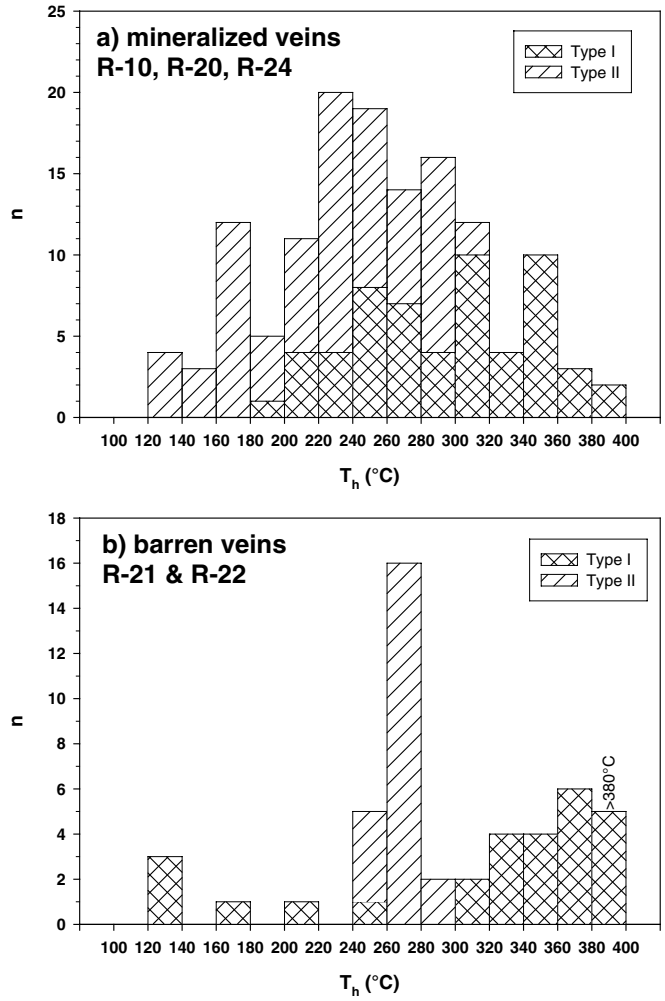

FIG. 13. Histograms showing temperatures of final homogenization (T_h; L → V) for samples from Um Egat. (a) Mineralized samples. (b) Barren veins.

conditions of fluid entrapment. The bimodal distribution of T_h values for each of the aqueous and carbonic inclusions can be used to group these inclusions into four categories: (1) type Ia carbonic inclusions with T_h = 200°–300°C (mostly ~250°C); (2) type Ib carbonic inclusions with T_h >300°C or failing to homogenize at T ~400°C; (3) type IIa aqueous inclusions with T_h of 220°–280°C; (4) type IIb aqueous inclusions with T_h <200°C (mostly between 150° and 200°C). It should be noted that type IIb inclusions occur only along secondary trails that crosscut grain boundaries.

The lack of a carbonic liquid phase and the relatively high $Tm_{clathrate}$ values (<17°C, average ~11°C) recorded for type I inclusions from Um Egat (and to a lesser extent, Dungash), suggest that the amount of CH_4 must have been large enough in some of the vein fluids (or parts thereof, e.g., R-10) to cause the disappearance of the three-phase field of two liquids and a carbonic vapor (Diamond, 2003). This conclusion is supported by some of our micro-Raman results (e.g., Fig. 15a), the "H2 type" behavior of these inclusions upon heating (cf. van den Kerkhof and Thiery, 2001), and by their relatively low initial ice-melting temperature (Tm_e ~ –64°C). Based on our micro-Raman results and the V-X diagrams of Thiery et al. (1994), the vapor composition of these carbonic inclusions is estimated at XCO_2 = 0.49, XCH_4 = 0.49, XN_2 = 0.02, for the Um Egat samples R-10 and R-20, and XCO_2 = 0.9, XCH_4 = 0.1 for Dungash samples 326 and 324.

Type III inclusions also contain $H_2O + CO_2 + CH_4 \pm N_2$ (Fig. 15f). However, the three-phase nature of these inclusions can be interpreted as indicative of either a CO_2/CH_4 ratio different from the two-phase type I carbonic inclusions, or their entrapment under different (lower P and T) conditions. On the other hand, micro-Raman analysis of type II inclusions, combined with their Tm_e and Tm_f values, suggests that they are filled with low salinity aqueous fluids belonging to the system H_2O-NaCl-CO_2 (Fig. 15b, c, e).

Attempts at modeling fluid compositions for type I carbonic inclusions using program "Bulk" of Bakker (2003), the equations of state of Bowers and Helgeson (1983) and Bakker (1999), T_h and Tm_f values, and assuming a vapor composition of XCO_2 = 0.49, XCH_4 = 0.49, XN_2 = 0.02, for the Um Egat samples R-10 and R-20, and XCO_2 = 0.9, XCH_4 = 0.1 for Dungash samples failed to yield any meaningful results. On the other hand, compositions for some type III inclusions from sample R-21 were modeled using routine "ICE" of the

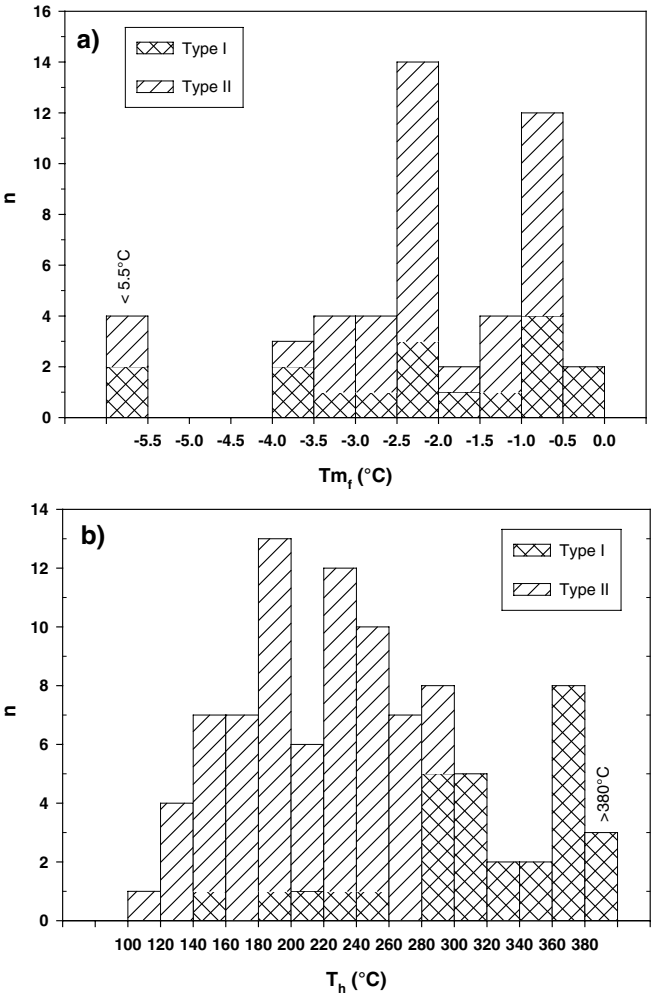

FIG. 14. (a) Histogram showing temperatures of final ice melting (Tm_f) for samples from Dungash. (b) Histogram showing temperatures of final homogenization (T_h; L → V) for samples from Dungash.

program "Clathrates" of Bakker (1997). Calculated densities ranged from 0.8 to 0.91 g/cm^3, with XCO_2 = 0.02–0.028, XCH_4 = 0.002–0.007, and XNa^+ <0.02.

Fluid compositions for the aqueous inclusions were modeled using program "Bulk" of Bakker (2003), the equations of state of Bowers and Helgeson (1983) and Bakker (1999), and values of Tm_f, T_h and vol percent of the liquid as recorded for each inclusion. Both type IIa and b inclusions had very similar densities of 0.92 to 0.99 g/cm^3 and molar volumes of 19.6 to 21 cm^3/ mol. With the exception of the Dungash fluids being slightly more saline, the compositions of these inclusions were almost the same from both areas, with XCO_2 = 0.03 – 0.045 and XNa^+ < 0.027. Modeling the few odd inclusions which homogenized through the disappearance of the liquid (L → V) yielded compositions of XCO_2 = 0.12–0.26, XNa^+ < 0.003, and densities of 0.27 to 0.89 g/cm^3.

Discussion and interpretation of microthermometric and modeling results

The occurrence of aqueous, aqueous-carbonic, and carbonic fluid inclusions in the same sample is typically explained by three possible processes.

1. One process is phase separation followed by heterogeneous entrapment of a CO_2 (± CH_4)-rich phase and a H_2O-rich one as carbonic and aqueous inclusions, respectively, as suggested by Robert and Kelly (1987), Sherlock et al. (1993), Dugdale and Hagemann (2001), and Neumayr and Hagemann (2002) for several different gold deposits from western Australia and Canada.

2. A second process is mixing of fluids from two different sources followed by entrapment of the mixtures as fluid inclusions (e.g., Xavier and Foster, 1999), and/or entrapment of different fluids at different times (e.g., Neumayr and Hagemann, 2002).

3. A third process is post-entrapment deformation affecting fluid inclusions that had formed by entrapment of a homogeneous (entirely miscible) phase at an earlier stage. In this case, deformation causes inclusions to stretch, leak, or decrepitate, resulting in the preferential loss of H_2O and the enrichment of the inclusions in CO_2 ± CH_4 (e.g., Hall and Sterner, 1993; Bakker and Jansen, 1994; Johnson and Hollister, 1995). The leaked H_2O-rich fluid is then trapped to form the aqueous inclusions.

Phase separation or CO_2 effervescence would necessitate that carbonic and aqueous inclusions occur in the same FIA, have widely varying degrees of fill, have a wide range of homogenization temperatures and compositions, and that pairs of liquid- and vapor-rich inclusions have opposite modes of homogenization (V → L, and L → V) in the same temperature range (e.g., Ramboz et al., 1982). Although aqueous and carbonic inclusions commonly coexist within the same field of view, and possibly belong to the same FIA in the veins of Um Egat and Dungash (e.g., Fig. 11c), the rarity of inclusions homogenizing through the disappearance of the liquid phase, coupled with the constant degree of fill for type II inclusions, led us to dismiss this process as the sole mechanism responsible for the formation of all types of fluid inclusions observed.

On the other hand, mixing of two separate fluids would result in an array of fluid inclusions with widely variable Tm_f and T_h values (reflecting variable compositions and temperatures of entrapment; e.g., Xavier and Foster, 1999). This is clearly not the case in the samples studied, which are characterized by uniform Tm_f values and clustering of T_h values into three groups (e.g., Figs. 12–14). Similarly, deformation-induced post-entrapment modification of inclusions originally formed by homogeneous entrapment of a fluid cannot solely account for all our observations, as this would also be expected to produce inclusions with a range of compositions and/or a scatter in homogenization temperatures that is larger than observed.

Figures 13 and 14 show that most type Ia and IIa inclusions have similar T_h (~250° ± 50°C) and often occur within the same FIA (e.g., Fig. 11c), which suggests that they formed simultaneously in the same sample. Heterogeneous entrapment after a stage of phase separation is therefore invoked to explain the coexistence of aqueous and carbonic inclusions with similar T_h values (type Ia and IIa inclusions). This would also account for the observed variation in the relative abundance of aqueous and carbonic inclusions from one sample to another even within the same vein. The occurrence of a few inclusions that homogenize through the disappearance of the

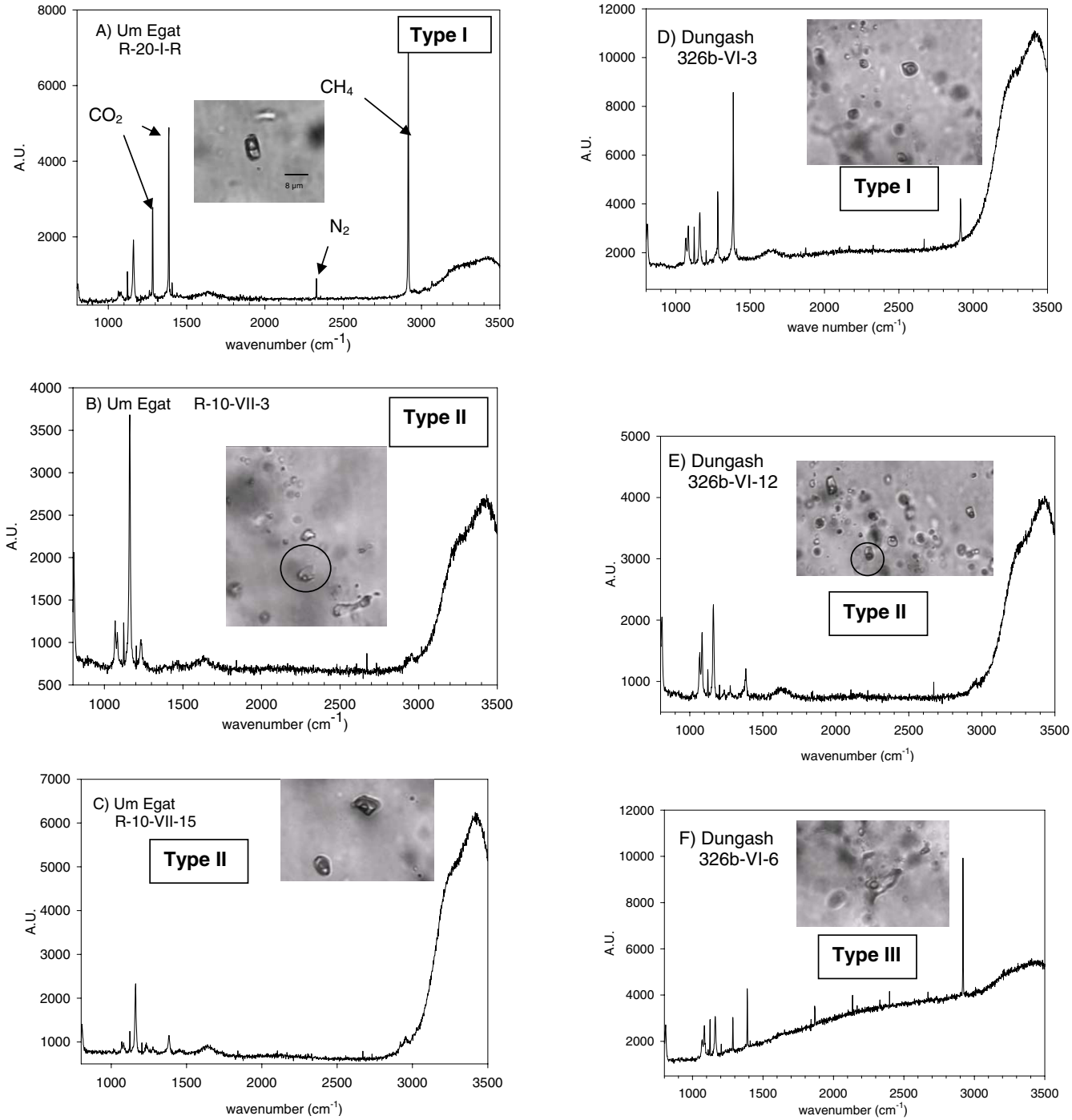

FIG. 15. Laser micro-Raman spectra for fluid inclusions representative of the various types described from Um Egat (a through c) and Dungash (d through f). All spectra plot wavenumbers against absorption units (A.U.).

liquid can also be explained by phase separation and heterogeneous entrapment.

Plots of T_h versus Tm_f show a weak negative trend for type Ia (and to a lesser extent, IIa) inclusions in both Um Egat and Dungash (Fig. 16). On the other hand, data for type IIb inclusions either define a distinct cluster (Fig. 16a) or a separate negative trend (e.g., Fig. 16b), whereas those for type Ib are quite scattered (Fig. 16). These patterns suggest that post-entrapment deformation played some role in fluid inclusion behavior by causing some of these inclusions to stretch and/or leak. Leakage causes the preferential loss of H_2O from aqueous-carbonic inclusions, which in turn results in an increase in fluid salinity and $XCO_2 \pm XCH_4$ (e.g., Hall and Sterner, 1993; Bakker and Jansen, 1994; Johnson and Hollister, 1995), whereas stretching causes an increase in inclusion volume (manifested by higher T_h; e.g., Vityk and Bodnar, 1995; Barker, 1995).

Accordingly, our data led us to the preliminary conclusion that type Ia and IIa inclusions formed simultaneously at

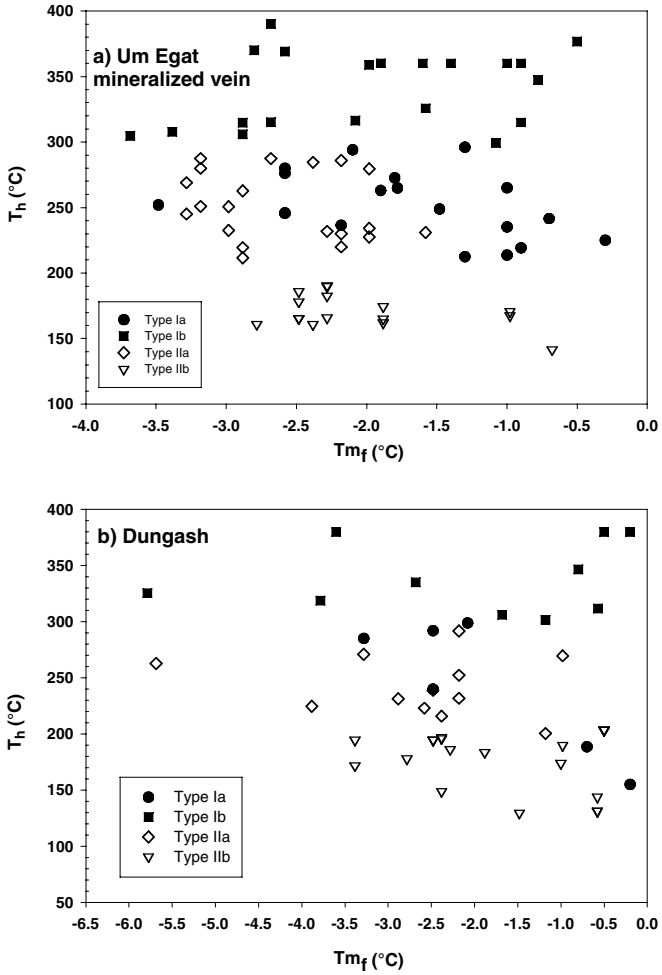

FIG. 16. Plots of final melting of ice temperatures versus homogenization temperatures for the different types of inclusions from samples from (a) Um Egat and (b) Dungash.

~250°C following a stage of phase separation at P <2.3 kbars (e.g., Crawford, 1981; Diamond, 2003) induced by a drop in P and T in the shear zones. Following heterogeneous entrapment of the carbonic and aqueous fluids, the vein was deformed, as evidenced by textures characteristic of semibrittle flow (e.g., grain bulging and deformation banding: Fig. 9a-c; cf. Tullis, 2002). This deformation caused some of the larger type Ia and IIa inclusions to stretch, leak, or decrepitate, and resulted in the observed scatter in their T_h and Tm_f values. Stretching and preferential loss of H_2O through leakage from some of the larger type Ia inclusions also led to the formation of some type Ib inclusions with negative crystal shapes and T_h >300°C (Fig. 16).

The three-phase aqueous-carbonic type III inclusions formed by the entrapment of an aqueous fluid with small amounts of dissolved $CO_2 \pm CH_4$ that may have been released from decrepitated and/or leaked aqueous and carbonic inclusions similar to types Ia and IIa. Alternatively, type III inclusions may have trapped an extraneous fluid introduced into these veins at a later stage of their evolution and at temperatures and pressures lower than those of entrapment of types Ia and IIa. Again, it may be that aqueous type IIb inclusions with their low T_h and constant degree of fill can be interpreted to have formed by trapping a different low-salinity aqueous fluid at considerably lower temperatures (200°–170°C) after the veins had undergone considerable cooling, fracturing, and healing of these fractures.

Accepting that type Ia, Ib, and IIa inclusions record evidence of heterogeneous entrapment after phase separation and post-entrapment deformation, their microthermometric data cannot directly constrain their P-T conditions of entrapment. However, some of these inclusions are identified as having been unaffected (or least affected) by post-entrapment deformation. The homogenization temperature for such inclusions would correspond to the temperature of immiscibility and could therefore be interpreted as the maximum temperature of entrapment (e.g., Ramboz et al., 1982; Uemoto et al., 2002). Because type IIa inclusions show the least amount of scatter in their T_h and Tm_f values (~250°C and –2.5°C, respectively; Fig. 16) they are considered to have been least affected by deformation. Isochores calculated for these inclusions could therefore be useful in constraining maximum pressures of entrapment, assuming that they formed simultaneously with type Ia at ~250°C.

Isochores for type IIa inclusions calculated using Bakker's (2003) program, "Isochore," show that their maximum pressure of entrapment (and hence minimum pressure of phase separation) was ~1.5 kbars for Um Egat and ~1.6 kbars for Dungash (Fig. 17). For such P-T conditions of entrapment, available data on the CO_2-H_2O–NaCl system (e.g., Crawford, 1981) and the effect of CH_4 on the miscibility gap (e.g., Diamond, 2003) suggest that XH_2O of the corresponding carbonic fluid trapped simultaneously in type Ia inclusions would be <0.3. Figure 17 also shows that the temperatures of fluid entrapment are considerably lower than the temperatures obtained by either arsenopyrite or chlorite geothermometry in both areas, indicating that phase separation postdated both the precipitation of ore minerals and the wall-rock alteration, and was probably not related to these two processes.

Although type III and IIb inclusions were unrelated to phase separation or post-entrapment deformation, they are still not useful for constraining the conditions of veining or gold precipitation. In the case of type III inclusions, their decrepitation rather than total homogenization precluded the calculation of accurate isochores, whereas for type IIb, their occurrence along late secondary trails interpreted to have developed after the entrapment of type I and IIa inclusions suggests that their formation was also unrelated to gold precipitation or remobilization or even chloritization of the wall rock (Fig. 17).

Origin and Evolution of the Gold-Bearing Fluids

The gold deposits of Um Egat and Dungash have similar metamorphic, structural, and mineralogical features that are characteristic of orogenic type deposits (Groves et al., 1998, 2003). Both deposits occur along shear zones that cut across the granitic intrusions of the Eastern Desert. These deposits are therefore not genetically related to the intrusion of the gray or pink granites, but instead are interpreted to have developed late in the orogenic cycle of the Arabian Nubian shield (e.g., Botros, 2004, and references therein). Because

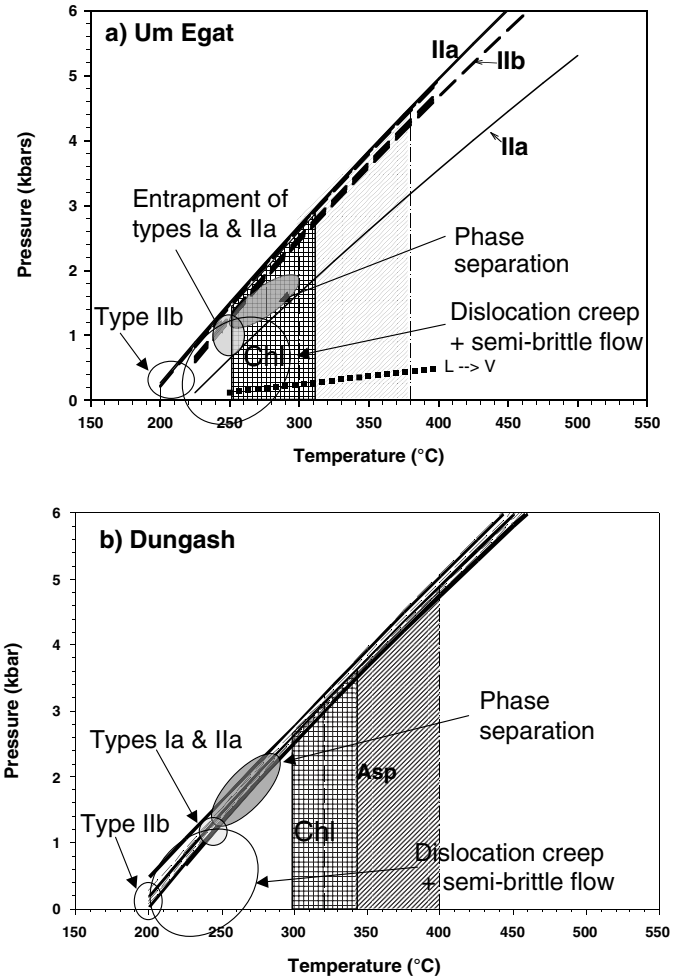

FIG. 17. Interpreted P-T evolution of the vein systems in (a) Um Egat and (b) Dungash. Solid lines are isochores for type IIa inclusions, dashed lines for type IIb; dotted line in (a) represents an isochore for an inclusion that homogenizes through the disappearance of the liquid (L → V). The stippled field outlined with dash-dotted lines delineates the temperatures inferred for the precipitation of arsenopyrite; the hachured field outlined with solid lines indicates that of chloritization of the wall rock. Ovals show schematically the conditions of phase separation, entrapment of type Ia and IIa inclusions, vein deformation, and entrapment of type IIb inclusions.

east-west–trending shear zones in the Eastern Desert crosscut and displace the pink granites along the Idfu-Mersa Alam road, whereas the northwest-southeast–trending structures only crosscut the older gray granite, the Dungash deposit is probably considerably younger than that of Um Egat. Nevertheless, both deposits have so many similarities that a single genetic model can adequately explain their origins.

Following regional metamorphism of arc-related volcanic rocks and their associated sediments under amphibolite to greenschist facies conditions and the intrusion of the older granites, major shear zones developed. Hot, low-salinity, aqueous fluids circulated through the shear zones. These fluids were probably derived from deeply buried (still unexhumed) volcanic and sedimentary rocks as they were being metamorphosed under amphibolite facies conditions while their shallow level counterparts (the present-day host rocks) were only metamorphosed under greenschist facies. Although a relationship between the mineralizing fluids and later intruding magmas (now represented by the younger pink granites) cannot be ruled out (e.g., Almond et al., 1984), it is more likely that these fluids were produced by regional metamorphism of the rocks hosting the gold-bearing veins. Two-dimensional thermal modeling by Stüwe et al. (1993) has shown that rapid erosion during metamorphism produces a cooling pile of low-grade metamorphic rocks overlying another pile that is still undergoing prograde metamorphism. This ultimately results in a time gap of 20 to 50 m.y. between metamorphism of the low-grade (host) rocks and their infiltration by mineralizing fluids generated from the underlying rock pile.

As these fluids migrated through graphite-bearing schists, they formed $CH_4 + CO_2$ according to the reaction $2\ H_2O + 2\ C = CH_4 + CO_2$ at $T \geq 400°C$ and $P > 3$ kbars (e.g., Johnson et al., 1992). Small amounts of N_2 were acquired from the dewatering of the volcanic and siliciclastic rocks (Jia and Kerrich, 1999) or the breakdown of $(NH_4)^+$-bearing micas and feldspars in the country rocks during metamorphism or hydrothermal alteration (Dubessy and Ramboz, 1986). Although the addition of $CH_4 \pm N_2$ to the fluid expands the solvus between the aqueous and carbonic phases (e.g., Naden and Shepherd, 1989), at these relatively high temperatures (>400°C), CO_2, CH_4, N_2 and H_2O were still completely miscible (e.g., Crawford, 1981; Diamond, 2003). The relatively reducing nature of these fluids allowed them to leach gold more efficiently from the mafic and ultramafic country rocks (e.g., Botros, 2004), carrying it in the form of bisulfide rather than chloride complexes (e.g., Sherlock et al., 1993; Mikucki, 1998).

As the aqueous-carbonic fluids migrated to shallower depths through the shear zones, they reacted with the country rocks over a wide range of temperatures (400°–240°C) forming the sericite, carbonate, and chlorite alteration zones, respectively (Helba et al., 2001). The carbonatization of the mafic country rocks triggered the precipitation of gold-bearing pyrite and arsenopyrite at temperatures of ~400° to 300°C in the carbonate-sericite zones, and led to the release of H^+ into the vein fluids (Mikucki, 1998). Increased H^+ concentration in the fluids led to more sericitization of the country rocks, and destabilized bisulfide complexes, which in turn led to the precipitation of free gold in the vein and altered wall rocks.

Opening and widening of the shear zones coupled with the upward migration of the fluids resulted in a drop of pressure and the subsequent separation of a carbonic phase and an aqueous phase at temperatures of ~250°C and $P \leq 2.3$ kbars (Fig. 17). Quartz crystallizing close to this P-T range trapped the carbonic and aqueous phases as discrete inclusions (types Ia and IIa) at depths of ~3 to 5 km. At the brittle-ductile transition, grain boundary bulging, deformation banding, subgrain rotation crystallization, and incipient annealing, all of which are known to occur at $T < 310°C$ and $P < 3$ kbars (e.g., Dunlap et al., 1997; Hirth et al., 2001; Stipp et al., 2002), resulted in variable degrees of stretching, necking down, leakage, and decrepitation of some inclusions. This stage was probably accompanied by recrystallization of arsenopyrite and pyrite and the remobilization of gold to secondary sites. As the temperature dropped below 200°C, microfractures

developed in vein quartz, and were subsequently healed, trapping H_2O-rich fluids in type IIb inclusions.

Conclusions

Um Egat and Dungash are orogenic gold deposits (Groves et al., 1998) and are quite similar to many Archean and later mesothermal vein-type deposits (e.g., Val d'Or, Quebec: Sherlock et al., 1993, and Neumayr and Hagemann, 2002; Golden Crown and Bronzewing, Western Australia: Uemoto et al., 2002, and Dugdale and Hagemann, 2001, Dongping deposit, China: Mao et al., 2003). In all these deposits, gold occurs in shear-related quartz veins or altered (typically carbonatized) greenschist facies host rocks. Fluid inclusions in vein quartz from these deposits all suggest an important role for low-salinity, $CO_2 \pm CH_4$-bearing fluids in the transport and/or precipitation of gold. Many of these veins also seem to have trapped more than one type of fluid at different times, with the latest postmineralization fluids usually being aqueous (e.g., Sigma mine, Quebec: Neumayr and Hagemann, 2002; this study). Commonly in such deposits, phase separation is invoked to explain the coexistence of aqueous and carbonic inclusions and is sometimes inferred to have played a role in the precipitation of gold (e.g., Dugdale and Hagemann, 2001; Uemoto et al., 2002).

The results of our study show that the precipitation of gold was triggered by reactions between fluid in the shear zones and the country rock at temperatures of ~300° to 400°C. Although the shear zones at Um Egat and Dungash have different trends, ages, and sense of shear, the vein-forming fluid in both areas had similar composition. Fluid immiscibility, which occurred as the temperature dropped to ~250°C or less, was therefore unrelated to the precipitation of any of the ore minerals. Semibrittle deformation of the vein quartz led to stretching, leakage, and decrepitation of some fluid inclusions. Late-stage deformation and incipient recovery of vein quartz resulted in the entrapment of different aqueous-carbonic and aqueous fluids, many along secondary trails, and in the remobilization of gold, causing its precipitation in secondary sites.

Acknowledgments

This study was made possible by grants from the German Academic Exchange Service (DAAD) to BZ and KIK, and a research grant from the University of Tennessee at Martin to AES. This work would not have been possible without the help and guidance of Dr. V. B. Sisson. The authors also acknowledge the technical support of Charles Farley with the micro-Raman analyses. Microprobe analyses were carried out on a CAMECA SX100 electron microprobe at the Institut fur Mineralogie und Mineralisches Rohstoffe, Technische Universitat, Clausthal, Germany (Dungash samples), and a JEOL JSM-6310 electron microprobe at the Institute of Geology and Mineralogy, Graz University, Austria (Um Egat).

May 17, 2006; February 28, 2008

REFERENCES

Afifi, A.M., and Essene, E.J., 1988, MINFILE: A microcomputer program for storage and manipulation of chemical data on minerals, American Mineralogist, v. 73, p. 446–447.

Almond, D.C., Ahmed, F., and Shaddad, M.Z., 1984, Setting of gold mineralization in the northern red Sea hills of Sudan: ECONOMIC GEOLOGY, v. 79, p. 389–392.

Amin, M.S., 1955, Geological features of some mineral deposits in Egypt: Desert Institute Bulletin, v. 5, p. 208–239.

Bakker, R.J., 1997, CLATHRATES: Computer programs to calculate fluid inclusion V-X properties using clathrate melting temperatures, Computers and Geosciences, v. 23, p. 1–18.

——1999, Adaptation of the Bowers and Helgeson (1983) equation of state to the H_2O-CO_2-CH_4-N_2-NaCl system, Chemical Geology, v. 154, p. 225–236.

——2003, Package FLUIDS 1. Computer programs for analysis of fluid inclusion data and for modelling bulk fluid properties: Chemical Geology, v. 194, p. 3–23.

Bakker R.J., and Jansen J.B.H., 1994, A mechanism for preferential H_2O leakage from fluid inclusions in quartz, based on TEM observations: Contributions to Mineralogy and Petrology, v. 116, p. 7–20.

Barker, A.J., 1995, Post-entrapment modification of fluid inclusions due to overpressure: Evidence from natural samples, Journal of Metamorphic Geology: v. 13, p. 737–750.

Botros, N.S., 2002, Metallogeny of gold in relation to the evolution of the Nubian Shield in Egypt: Ore Geology Reviews, v. 19, p. 137–164.

——2004, A new classification of the gold deposits of Egypt. Ore Geology Reviews, v. 25, p. 1–37.

Bowers, T.S., and Helgeson, H.C., 1983, Calculation of thermodynamic and geochemical consequences of nonideal mixing in the system H_2O-CO_2-NaCl on phase relations in geologic systems: Equation of state for H_2O-CO_2-NaCl fluids at high pressures and temperatures: Geochimica et Cosmochimica Acta, v. 47, p. 1247–1275.

Cathelineau, M., 1988, Cation site occupancy in chlorites and illites as a function of temperature: Clay Minerals, v. 23, p. 471–485.

Crawford, M.L., 1981, Fluid inclusions in metamorphic rocks-low and medium grade, *in* Hollister, L.S., and Crawford, M.L., eds., Fluid inclusions: Applications to petrology: Mineralogical Association of Canada, Short Course Handbook, v. 6, p. 157–181.

Diamond, L.W., 2003, Introduction to gas bearing, aqueous fluid inclusions, *in* Samson, I., Anderson, A., and Marshall, D., eds. Fluid inclusions: Analysis and interpretation: Mineralogical Association of Canada, v. 32, p. 101–158.

Dubessy, J., and Ramboz, C., 1986, The history of organic nitrogen from early diagenesis to amphibolite facies: Mineralogical, chemical, mechanical, and isotopic implications: International Association of Geochemistry (IAGC), Fifth International Symposium on Water-Rock Interaction: Reykjaveik, Extended Abstracts, p. 170–174.

Dugdale, A.L., and Hagemann, S.G., 2001, The Bronzewing lode-gold deposit, Western Australia: P-T-X evidence for fluid immiscibility caused by cyclic decompression in gold-bearing quartz veins: Chemical Geology, v. 173, p. 59–90.

Dunlap, W., Hirth, G., and Teyssier, C., 1997, Thermomechanical evolution of a ductile complex: Tectonics, v. 16, p. 983–1000.

Egyptian Mineral Resources Authority, 2006, International bid round report 2006, Part II: Potentiality of bid round blocks, Report distributed by the Egyptian Mineral Resource Authority, Egyptian Ministry of Petroleum, 53 p. (http://www.egsma.gov.eg/sss/Part%20II.pdf)

El Gaby, S., List, F.K., and Tehrani, R., 1988, Geology, evolution, and metallogenesis of Pan-African belt in Egypt, *in* El-Gaby, S., and Greiling, R.O., eds., The Pan-African belt of northeast Africa and adjacent areas: Braunschweig, Freidr, Vieweg, & Sohn, p. 17–68.

——1990, The basement complex of the Eastern Desert and Sinai, *in* Said, R., ed., The geology of Egypt: Rotterdam, Balkema, p. 175–184.

El-Ramly, M.F., Ivanov, S.S., and Kochin, G.C., 1970, The occurrence of gold in the Eastern Desert of Egypt: Geological Survey of Egypt, Studies on some mineral deposits of Egypt: Metallic Minerals, Part I, Sec. A, v. 21, p. 1–22.

El-Shazly, A.K., and Sisson, V.B., 2004, Fluid inclusions in carpholite-bearing metasediments and blueschists from NE Oman: Constraints on P-T evolution: European Journal of Mineralogy, v. 16, p. 221–233.

El-Shazly, E.M., 1957, Classification of Egyptian mineral deposits: Egyptian Journal of Geology, v. 1, p. 1–20.

El Shimi, K.A., 1996, Geology, structure and exploration of gold mineralization in Wadi Allaqi area (SW, Eastern Desert, Egypt): Unpublished Ph.D. thesis, Cairo, Ain Shams University, 326 p.

Greaves, R.H., and Little, O.H., 1929, The gold resources of Egypt: International Geological Congress, South Africa, Gold Resources of the World, v. 11, p. 123-126.

Groves, D.I., Goldfarb, R.J., Gebre-Mariam, M., Hagemann, S.G., and Robert, F., 1998, Orogenic gold deposits: A proposed classification in the

context of their crustal deformation and relationship to other gold deposit types: Ore Geology Reviews, v. 13, p. 7–28.

Groves, D.I., Goldfarb, R.J., Robert, F., and Hart, C.J.R., 2003, Gold deposits in metamorphic belts: Overview of current understanding, outstanding problems, future research, and exploration significance: Economic Geology, v. 98, p. 1–29.

Hall, D.L., and Sterner, M.S., 1993, Preferential water loss from synthetic fluid inclusions: Contributions to Mineralogy and Petrology, v. 114, p. 489–500.

Harraz, H.Z., 2000, A genetic model for a mesothermal Au deposit: Evidence from fluid inclusions and stable isotopic studies at El-Sid gold mine, Eastern Desert: Journal of African Earth Sciences, v. 30, p. 267–282.

——2002, Fluid inclusions in the mesothermal gold deposit at Atud mine, Eastern Desert, Egypt: Journal of African Earth Sciences, v. 35, p. 347–363.

Harraz, H.Z., and Ashmawy, M.H., 1994, Structural and lithogeochemical constraints on the localization of gold deposits at the El Sid-Fawakhir gold mine area, Eastern Desert, Egypt: Egyptian Journal of Geology, v. 38, p. 629–648.

Hassaan, M.M., and El-Mezayen, A.M., 1995, Genesis of gold mineralization in Eastern Desert, Egypt: Al-Azhar Bulletin of Science, v. 6, p. 921–939.

Hassan, M.A., and Hashad, A.H., 1990, Precambrian of Egypt, *in* Said, R., ed., The geology of Egypt: Rotterdam, Balkema, p. 201–245.

Helba, H.A., Khalil, K.I., and Abdou, N.M., 2001, Alteration patterns related to hydrothermal gold mineralization in meta-andesites at Dungash area, Eastern Desert, Egypt: Resource Geology, v. 51, p. 19–30.

Hirth, G., Teyssier, C., and Dunlap, W.J., 2001, An evaluation of quartzite flow laws based on comparisons between experimentally and naturally deformed rocks: International Journal of Earth Sciences, v. 90, p. 77–87.

Hussein, A.A., 1990, Mineral deposits, *in* Said, R., ed., The geology of Egypt: Rotterdam, Balkema, p. 511–566.

Jia, Y., and Kerrich, R., 1999, Nitrogen isotope systematics of mesothermal lode gold deposits: Metamorphic, granitic, meteoric water, or mantle origin: Geology, v. 27, p. 1051–1054.

Johnson, E.L., and Hollister, L.S., 1995, Syndeformational fluid trapping in quartz: Determining the pressure-temperature conditions of deformation from fluid inclusions and the formation of pure CO_2 fluid inclusions during grain boundary migration: Journal of Metamorphic Geology, v. 13, p. 239–249.

Johnson, J.W., Oelkers, E.H., and Helgeson, H.C., 1992, SUPCRT 92: A software package for calculating the standard molal thermodynamic propserties of minerals, gases, aqueous species, and reactions from 1 to 5000 bars and 0° to 1000°C: Computers and Geosciences, v. 18, p. 899–947.

Khalil, K.I., Helba, H.A., and Mucke, A., 2003, Genesis of the gold mineralization at the Dungash gold mine area, Eastern Desert, Egypt: A mineralogical-microchemical study: Journal of African Earth Sciences, v. 37, p. 111–122.

Klemm, D.D., 1965, Synthesen und analysen in den dreicksdiagrammen FeAsS-CoAsS-NiAsS und FeS_2-CoS_2-NiS_2: Neues Jahrbuch für Mineralogie, v. 103, p. 205–255.

Klemm, D.D., Klemm, R., and Murr, A., 2001, Gold of the Pharaohs—6000 years of gold mining in Egypt and Nubia: Journal of African Earth Sciences, v. 33, p. 643–659.

Kochine, G.G., and Bassuni, F.A., 1968, Mineral resources of the U.A.R.: Part I. Metallic minerals: Internal Report, Geological Survey of Egypt, p. 305–436.

Kranidiotis, P., and MacLean, W.H., 1987, Systematics of chlorite alteration at the Phelps Dodge massive sulfide deposit, Matagami, Quebec, Economic Geology, v. 82, p. 1898–1911.

Kretschmar, U., and Scott, S D., 1976, Phase relations involving arsenopyrite in the system Fe-As-S and their application: Canadian Mineralogist, v. 14, p. 364–386.

Lang, J.R., and Baker, T., 2001, Intrusion related gold systems—the present level of understanding: Mineralium Deposita, v. 36, p. 477–489.

Loizenbauer, J., and Neumayr, P., 1996, Structural controls on the formation of the Fawakhir gold mine, EL Sid-Eastern Desert, Egypt: Tectonic and fluid inclusion evidence: Proceedings of the Geological Survey of Egypt Centennial Conference, p. 477–488.

Mao, J., Li, Y., Goldfarb, R., He, Y., and Zaw, K., 2003, Fluid inclusion and noble gas studies of the Dongping gold deposit, Hebei province, China: Mantle connection for mineralization?: Economic Geology, v. 98, p. 517–534.

Mikucki, E.J., 1998, Hydrothermal transport and depositional processes in Archean lode-gold systems: A review: Ore Geology Reviews, v. 13, p. 307–321.

Morgan, P., 1990, Egypt in the framework of global tectonics, *in* Said, R., ed., The geology of Egypt: Rotterdam, Balkema, p. 91–111.

Naden, J., and Shepherd, T.J., 1989, Role of methane and carbon dioxide in gold deposition: Nature, v. 342, p. 793–795.

Neumayr, P., and Hagemann, S., 2002, Hydrothermal fluid evolution within the Cadillac tectonic zone, Abitibi greenstone belt, Canada: Relationship to auriferous fluids in adjacent second and third-order shear zones: Economic Geology, v. 97, p. 1203–1225.

Oweiss, Kh. A., and Said, M.M., 2000, Geological and geochemical exploration for gold at Um Egat (Al Fawi) area, south Eastern Desert, Egypt: Annals of the Geological Survey of Egypt, v. 23, no. 2, p. 609–613.

Pohl, W., 1988, Precambrian Metallogeny of NE-Africa, *in* El Gaby, S., and Greiling, R. O., eds., The Pan-African belt of NE Africa and adjacent areas: Wiesbaden, Earth Evolution Science, p. 319–341.

Ramboz, C., Pichavant, M., and Weisbrod, A., 1982, Fluid immiscibility in natural processes: Use and misuse of fluid inclusion data: II. Interpretation of fluid inclusion data in terms of immiscibility: Chemical Geology, v. 37, p. 29–48.

Robert, F., and Kelly, W.C., 1987, Ore forming fluids in Archean gold-bearing quartz veins at the Sigma mine, Abitibi greenstone belt, Quebec. Part I. Geologic relations and formation of the vein system: Economic Geology, v. 81, p. 587–592.

Sabet, A.H., and Bondonosov, V.P., 1984, The gold ore formations in the Eastern Desert of Egypt: Annals of the Geological Survey of Egypt, v. 14, p. 35–42.

Scott, S.D., 1983, Chemical behaviour of sphalerite and arsenopyrite in hydrothermal and metamorphic environments: Mineralogical Magazine, v. 47, p. 427–435.

Sherlock, R.L., Jowett, C.E., Smith, B.D., and Irish, D.E., 1993, Distinguishing barren and auriferous veins in the Sigma mine, Val-d'Or, Quebec: Canadian Journal of Earth Science, v. 30, p. 413–419.

Stern, R.J., 1981, Petrogenesis and tectonic setting of late Precambrian ensimatic volcanic rocks, central Eastern Desert of Egypt: Precambrian Research, v. 16, p. 195–230.

Stipp, M., Stunitz, H., Heilbronner, R., and Schmid, S., 2002, Dynamic recrystallization of quartz: Correlation between natural and experimental conditions: The Geological Society [London], Special Publications, v. 200, p. 171–190.

Stüwe, K., Will, T., and Zhou, S., 1993, On the timing relationship between fluid production and metamorphism in metamorphic piles: some implications for the origin of post-metamorphic gold mineralization: Earth and Planetary Science Letters, v. 114, p. 417–430.

Thiéry, R., van den Kerkhof, A.M., and Dubessy, J., 1994, *v-X* properties of CH_4-CO_2 and CO_2-N_2 fluid inclusions: Modeling for T <31°C and P <400 bars: European Journal of Mineralogy, v. 6, p. 753–777.

Tullis, J., 2002, Deformation of granitic rocks: Experimental studies and natural samples, *in* Karato, S-I., and Wenk, H-R., eds., Plastic deformation of minerals and rocks: Reviews in Mineralogy, v. 51, p. 51–95.

Uemoto, T., Ridely, J., Mikucki, E., and Groves, D.I., 2002, Fluid chemical evolution as a factor in controlling the distribution of gold at the Archean Golden Crown lode gold deposit, Murchison Province, Western Australia: Economic Geology, v. 97, p. 1227–1248.

van den Kerkhof, A., and Thiery, R., 2001, Carbonic inclusions, Lithos, v. 55, p. 49–68.

Vityk, M.O., and Bodnar, R.J., 1995, Do fluid inclusions in high-grade metamorphic terranes preserve peak metamorphic density during retrograde decompression?: American Mineralogist, v. 80, p. 641–644.

Xavier, R.P., and Foster, R.P., 1999, Fluid evolution and chemical controls in the Fazenda Maria Preta (FMP) gold deposit, Rio Itapicuru greenstone belt, Bahia, Brazil: Chemical Geology, v. 154, p. 133–154.

Zoheir, B.A., 2004, Gold mineralization in the Um El Tuyor area, south Eastern Desert, Egypt: Geologic context, characteristics and genesis: Unpublished Ph.D. thesis, Germany, Ludwig-Maximilians-Universität München, 159 p.

Zoheir, B.A., and Klemm, D.D., 2007, The tectonometamorphic evolution of the central part of the Neoproterozoic Allaqi-Heiani suture, south Eastern Desert of Egypt: Gondwana Research, v. 12, p. 287–304.